

# Electrochemical Nucleation of Lithium on Copper

Understanding of Nucleation in Future Lithium-Metal Batteries

Master's Thesis in Physics

GOTTFRID OLSSON

DEPARTMENT OF PHYSICS

CHALMERS UNIVERSITY OF TECHNOLOGY  
Gothenburg, Sweden 2024  
[www.chalmers.se](http://www.chalmers.se)



MASTER'S THESIS 2024

# **Electrochemical Nucleation of Lithium on Copper**

Understanding of Nucleation in Future Lithium-Metal Batteries

GOTTFRID OLSSON



Department of Physics  
*Division of Materials Physics*  
CHALMERS UNIVERSITY OF TECHNOLOGY  
Gothenburg, Sweden 2024

Electrochemical Nucleation of Lithium on Copper  
Understanding of Nucleation in Future Lithium-Metal Batteries  
GOTTFRID OLSSON

© GOTTFRID OLSSON, 2024.

Supervisor: Josef Rizell, Department of Physics  
Examiner: Alexander Matic, Department of Physics

Master's Thesis 2024  
Department of Physics  
Division of Materials Physics  
Chalmers University of Technology  
SE-412 96 Gothenburg

Cover: Electrochemical deposition of lithium (Li) in a Li and copper (Cu) cell where Li-ions ( $\text{Li}^+$ ) get deposited as Li onto the Cu, creating nuclei which grow as more charge is passed. The electron microscope image shows Li nuclei on the Cu.  
Cover figure created by Gottfrid Olsson.

Typeset in L<sup>A</sup>T<sub>E</sub>X  
Printed by Chalmers digitaltryck  
Gothenburg, Sweden 2024

Electrochemical Nucleation of Lithium on Copper  
Understanding of Nucleation in Future Lithium-Metal Batteries  
GOTTFRID OLSSON  
Department of Physics

## Abstract

Batteries are used for energy storage everywhere, from mobile phones and power tools to electric vehicles and in space exploration. Electrical vehicles, for example, would gain increased range from batteries with higher energy densities and higher specific energies. By replacing the graphite in today's widespread lithium-ion batteries with lithium (Li), the energy density of the cell can double from  $600 \text{ Wh L}^{-1}$  to  $1200 \text{ Wh L}^{-1}$  and the specific energy of the cell can increase from  $250 \text{ Wh kg}^{-1}$  to  $440 \text{ Wh kg}^{-1}$ . However, non-uniform deposition of Li during charging causes problems, including formation of "dead" Li leading to low Coulombic efficiency and a short cycle life, and is a safety risk by potentially short-circuiting the cell. To enable more uniform Li deposition, the first step during deposition – nucleation – needs to be better understood. This work studies nucleation of Li on a copper surface using electrochemical cycling and scanning electron microscopy. In particular, the effect of pressure, current density, and passivation of the copper surface are investigated.

Keywords: electrochemical nucleation, lithium nuclei, scanning electron microscopy, lithium-metal battery

## **Acknowledgements**

My gratitude goes out to my supervisor Josef Rizell, who not only taught me the essentials of battery research in the laboratory, but who was also always available for discussion and brightened each day with an encouraging and positive attitude. Moreover, I am thankful for the support of my examiner Aleksandar Matic, who helped guide this project with ideas and encouragement. I must also mention the lovely people of the material physics department – it has been wonderful to get to know and work with you. Lastly, I offer my thanks to the friends who have given constructive feedback on my figures, making them ever more elegant.

Gottfrid Olsson, Gothenburg, May 2024

# Contents

## Contents

<b>1</b>	<b>Introduction</b>	<b>1</b>
<b>2</b>	<b>Lithium batteries</b>	<b>3</b>
2.1	History of batteries and use today . . . . .	3
2.2	Battery concepts with a lithium-ion battery (LIB) example . . . . .	4
2.3	The lithium-metal battery (LMB) . . . . .	7
2.3.1	Problems with non-uniform lithium deposition . . . . .	8
<b>3</b>	<b>Nucleation</b>	<b>11</b>
3.1	Steps during nucleation and growth . . . . .	11
3.2	Deposition curve in a lithium/copper cell . . . . .	12
3.3	Homogenous nucleation theory . . . . .	14
3.4	Scientific questions addressed in this work . . . . .	16
<b>4</b>	<b>Methods</b>	<b>19</b>
4.1	Material preparation . . . . .	19
4.1.1	Electrode materials . . . . .	19
4.1.2	Electrolytes . . . . .	20
4.2	Cell configurations and assembly . . . . .	21
4.2.1	The coin cell (C-cell) . . . . .	22
4.2.2	The Swagelok two-electrode cell (I-cell) . . . . .	24
4.2.3	The Swagelok three-electrode cell (T-cell) . . . . .	26
4.3	Electrochemical cycling of the cells . . . . .	28
4.3.1	Cycling protocol for SEM images . . . . .	28
4.3.2	Cycling protocol for electrochemical measurements . . . . .	29
4.3.3	Sample preparation for SEM . . . . .	30
4.4	Electron microscopy . . . . .	30
4.4.1	The scanning electron microscope (SEM) . . . . .	31
4.5	Data analysis . . . . .	33

<b>5 Results and discussion</b>	<b>35</b>
5.1 Passivation of the Cu surface before deposition . . . . .	35
5.2 Deposition current density . . . . .	38
5.3 Comparison of different electrolytes . . . . .	41
5.4 Cell configuration and pressure . . . . .	43
5.4.1 Cell configuration effects on the deposition curve . . . . .	43
5.4.2 Pressure effects on the nuclei distribution . . . . .	45
<b>6 Conclusions</b>	<b>51</b>
<b>References</b>	<b>53</b>
<b>A Supplementary information: methods</b>	<b>I</b>
A.1 Polishing of Cu . . . . .	I
A.2 Polypropylene spacer for T-cell . . . . .	III
<b>B Supplementary information: results</b>	<b>V</b>
B.1 Experimental procedures to obtain clean SEM images of Li nuclei . . . . .	V
B.2 Influence of passivation of the Cu surface before deposition . . . . .	VIII

# Introduction

Batteries play an important role in our society, being used in things ranging from mobile phones, hearing aids and pacemakers [1], to power tools [2], emergency power [2], electric vehicles [3], and even in space exploration [4], [5]. Lithium-ion batteries (LIBs) are one of the most widely used types of batteries, with billions of cells being produced each year [6]. Despite the popularity of LIBs, the need for even better lithium-based batteries are growing due to increasing demands [3]. For example, electrical vehicles would gain the benefit of increased range from batteries with higher energy densities and higher specific energies [7]. One way to achieve higher energy density and specific energy is by replacing the graphite in a LIB with Li-metal. This replacement can double the energy density of the cell from  $600 \text{ Wh L}^{-1}$  to  $1200 \text{ Wh L}^{-1}$  [2] and increase the specific energy of from  $250 \text{ Wh kg}^{-1}$  to  $440 \text{ Wh kg}^{-1}$  [8]. However, such lithium-metal batteries (LMBs) have short cycle life and are a safety risk. When a LMB is charged, lithium (Li) gets deposited and grows directly on the electrode surface. Uneven growth of this Li leads to low Coulombic efficiency due to "dead" Li [9]–[12], a short cycle life [9], [10], and is a safety risk by enabling Li-growth that can short-circuit the cell [9]–[11]. This uneven deposition of Li is considered a large obstacle for practical application of Li-metal in batteries [12]–[14].

To solve the problem of uneven deposition, the process must first be well understood. Studies have been conducted on both the nucleation and growth of Li-metal [15]–[18]. The first step – nucleation of Li – is important since the initial nuclei distribution influences the growth and subsequent resulting morphology of the deposition as a whole. More knowledge about the process can therefore lead to ways of enabling more even and regular nucleation and growth in LMBs, which would

improve their cycle life and safety.

The purpose of this work is to investigate how the nucleation in Li-metal cells can be influenced. Specifically, electron microscopy will be used to image deposited Li in different cell configurations, and electrochemical cycling will be performed to investigate the nucleation behavior in different cell configurations as function of current density with different levels of passivation of the counter electrode surface.

# 2

## Lithium batteries

In this section, a short history of batteries and their use today is first given. Thereafter, fundamental battery concepts are explained, with an example of the LIB since it is both instructive and a common battery type. Relevant theoretical ideas are then introduced, such as the cell potential, Gibbs free energy, and overpotential, of which the last two will be central for understanding nucleation. Finally, a LMB example showcases problems associated with non-uniform deposition of Li.

### 2.1 History of batteries and use today

The history of batteries always starts with Alessandro Volta, who in 1800 created an "electric pile" in order to settle an intellectual dispute [1]. The pile was the world's first battery<sup>1</sup> and consisted of alternating disks of silver and zinc, with cloths soaked in salt water in between [1]. Volta's pile demonstrated that electrical energy could be stored in and extracted from metals and electrolytes (liquids with ions). Several different rechargeable batteries were invented thereafter, for instance the lead-acid battery (1859) [1], the nickel-cadmium battery (1901) [1], and the lithium-ion battery (1991<sup>2</sup>) [2]. These earlier types of batteries have been improved

---

<sup>1</sup>The word "battery" for such a device was coined by Benjamin Franklin (as a play on the military term) in 1748 when describing his experiments with an "electrical battery" [19]. Franklin's electrical battery consisted of eleven large glass panes, with lead on each side, placed close to each other in series (a series of capacitors) [19]. Others had experimented with electrical batteries before, most notably Johann Heinrich Winkler and Daniel Gralath, both in 1746 [19].

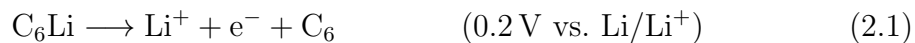
<sup>2</sup>The earliest functioning rechargeable lithium battery came during the 1970s. However, what we today call a rechargeable LIB was first patented in 1991 [20], by then standing on the shoulders of decades worth of lithium battery research [2], [20].

on during the years and are still in use today. For example, lead-acid batteries helps ignite car engines and drives industrial trucks [2], while nickel-cadmium batteries are used in power tools and as emergency power [2]. LIBs can be found everywhere, some examples already mentioned are in consumer electronics such as mobile phones, watches, and laptops, but LIBs are also used in power tools, electrical vehicles [1], and space exploration [4].

## 2.2 Battery concepts with a lithium-ion battery (LIB) example

A battery is a device consisting of several cells, where each cell stores chemical energy that can be extracted as electricity [21]. A cell, in turn, is made up of several parts, as illustrated in Figure 2.1. The electrode materials, here graphite and LiCoO<sub>2</sub> (LCO), are electrically conductive and provides the materials necessary for electrochemical reactions to occur. Between the electrodes is an electrolyte and a separator. The separator keeps the electrodes from touching each other and thereby short-circuiting, while the electrolyte prevents electrons ( $e^-$ ) from passing through, but allows ions (such as Li<sup>+</sup>), to move between the electrodes. The last components are the current collectors, here copper (Cu) and aluminium (Al), and the external circuit. Current collectors connect to each electrode, enabling the transportation of electrons from the electrode materials to the external circuit. The external circuit provides a way to connect the cell to a device, a load, thereby closing the circuit. The ions move between the electrodes through the electrolyte, and the electrons move from one electrode to the other through the current collectors and the external circuit.

Let us look at the example of the LIB cell in Figure 2.1 and its reduction-oxidation (redox) reactions. The cell is charged, meaning that Li are contained in the graphite. Since the cell is charged, energy has been put in to store the Li in the graphite, meaning that the Li have more energy in the graphite compared to what it had in the LCO. This extra energy can be extracted through discharging the cell by electrically connecting the electrodes through a load. From the charged state, Li in the graphite (C<sub>6</sub>) can be released and become a Li-ion (Li<sup>+</sup>) by giving away an electron according to



which is an oxidation reaction (since the C<sub>6</sub>Li loses an electron), and the electrical potential of this reaction is 0.2 V versus Li/Li<sup>+</sup>[22]. On the other side of the cell,

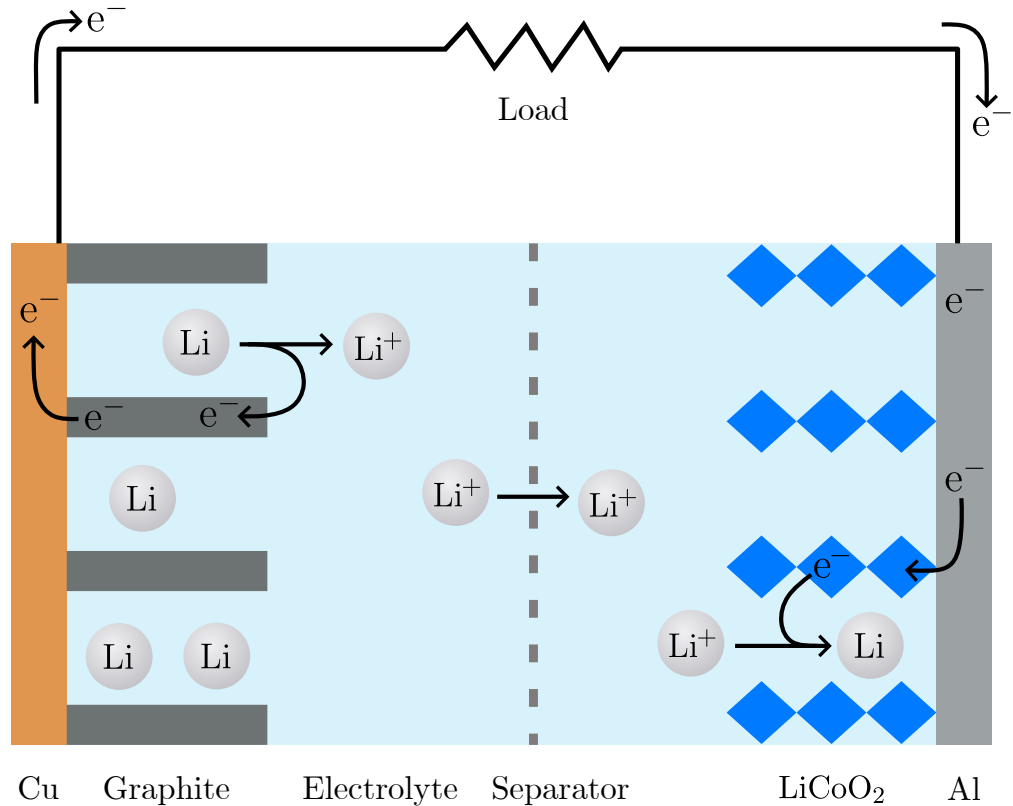


**Figure 2.1.** A schematic view of a cell in a LIB, showing the parts (not to scale) inside the cell casing during discharging. As an example, the electrodes are here graphite (each graphite layer is illustrated as gray rectangles) and LCO (blue rhombuses are CoO<sub>2</sub>-layers) which are commonly used in LIBs. The electrolyte (light blue background) enables transportation of ions, but not electrons, between the electrodes, and the separator (dashed gray line) keeps the electrodes from short-circuiting while letting  $Li^+$  through. The current collectors, Cu (brown rectangle) and Al (gray rectangle), collect and transport the electrons to the outer circuit where the load is.

the LCO can pick up a Li-ion and an electron according to



which is a reduction reaction (since the LCO gains an electron) and the potential is 4.1 V versus Li/Li<sup>+</sup>[23]. Combining these gives



which is a redox reaction. In this example, Li move out from the graphite and into the LCO during discharge, while the electrons at the same time move from

the graphite through the external circuit and load to the LCO. During charging, a voltage is applied to the cell and the arrows in the reactions above are flipped, indicating that reactions and movements of Li-ions and electrons are reversed.

To further understand batteries and later the nucleation, the concepts of cell potential, Gibbs free energy, and overpotential are needed. The voltage difference between the two electrodes in a cell, called the cell voltage, is given by

$$E_{\text{cell}} = E_{\text{reduction}} - E_{\text{oxidation}} \quad (2.4)$$

where  $E_{\text{reduction}}$  and  $E_{\text{oxidation}}$  are the potentials of the reduction and oxidation reaction, respectively. For our example in the LIB cell the overall redox reaction is given by Equation 2.3, and we get that  $E_{\text{cell}}^{\text{graphite/LCO}} = 3.9 \text{ V}$  using the reduction and oxidation potentials from Equation 2.1 and Equation 2.2, respectively. This result, despite coming from a simple calculation, corresponds well with real LIBs which most often operate at 3.8 V [24]. Also, current  $I$  ( $\text{A} = \text{Cs}^{-1}$ ), which describes the flow of charges, would in our example (approximately) describe how fast the redox reaction in Equation 2.3 occurs, with a higher current meaning more a higher reaction rate. In battery research, current is frequently expressed as a current density  $J$  ( $\text{A cm}^{-2}$ ), where the current is divided by the area of the relevant electrode.

The cell voltage can also be obtained theoretically using the change in Gibbs free energy. Gibbs free energy  $G$  describes the maximum amount of work a closed system can do (that is not pressure-volume work). This is relevant because the change in Gibbs energy  $\Delta G$  for a reaction dictates whether that reaction can occur spontaneously, if  $\Delta G < 0$ , or require external energy to happen, if  $\Delta G > 0$ . The voltage of a cell  $E_{\text{cell}}$  is related to  $\Delta G$  and the charge passed through the cell  $nF$  according to

$$\Delta G = -nFE_{\text{cell}} \quad (2.5)$$

where  $n$  is the number of moles of electrons included in the redox reaction and  $F = 96\,485 \text{ C mol}^{-1}$  is Faraday's constant (charge per mole of electrons) [25]. The negative sign takes into account that  $E_{\text{cell}} > 0$  when a cell is discharging, and since the redox reaction happen spontaneously it must hold that  $\Delta G < 0$ . The change in Gibbs free energy will be central when discussion nucleation.

The final relevant concept introduced here is overpotential, which has to do with the potential of reactions. As shown, a given oxidation or reduction reaction occurs at some potential. That potential can be calculated theoretically and is therefore called the theoretical equilibrium potential,  $E_{\text{equilibrium}}$ . The potential for which

the reaction occurs in practice is  $E$ , and the overpotential  $\eta$  is then given by

$$\eta = E - E_{\text{equilibrium}} \quad (2.6)$$

which describes how far away from equilibrium the reaction actually takes place [25]. One reason that  $E \neq E_{\text{equilibrium}}$  is that there is often an energy barrier that needs to be overcome in order for a reaction to occur. Also, a larger overpotential means there is a stronger driving force for the reaction, resulting in a larger current (higher reaction rate) in the case of an electrochemical cell. Overpotential plays an important role in nucleation, influencing both the size of Li nuclei and the number of nuclei per area [15].

We have now learned about the history of batteries, gone through an example of the widespread LIB and simultaneously explained many of the fundamental concepts in an electrochemical cell, as well as concepts relevant to nucleation. Now, let us move on to one of the battery types the next generation might use – the LMB.

## 2.3 The lithium-metal battery (LMB)

Li is considered one of the top candidates for high-energy batteries is due to its favorable properties. To understand this, the quantity capacity is introduced. Capacity is a material's ability to store charge and is measured in milliampere hours (1 mAh is equal to 3.6 C, or  $10^{19}$  electrons<sup>3</sup>). A material's specific capacity is its capacity divided by its mass ( $\text{mAh g}^{-1}$ ), and a high specific capacity means more energy stored per mass of material. Compared to all other elements, for example sodium (1166  $\text{mAh g}^{-1}$ ), potassium (685  $\text{mAh g}^{-1}$ ), nickel (457  $\text{mAh g}^{-1}$ ), cadmium (238  $\text{mAh g}^{-1}$ ) and lead (129  $\text{mAh g}^{-1}$ ), Li has the highest theoretical capacity<sup>4</sup> of 3860  $\text{mAh g}^{-1}$ . Li is a compelling candidate for high-energy batteries for this reason, and also for its other favorable properties like low standard electrode potential ( $-3.04$  V against the standard hydrogen electrode) [8] and low density ( $0.534 \text{ g cm}^{-3}$ , almost half that of water) [9]. The high theoretical capacity increases the specific energy ( $\text{Wh kg}^{-1}$ ) of the cell, while the low density of Li increases the energy density ( $\text{Wh L}^{-1}$ ) of the cell. Low standard electrode potential help increases both these quantities.

A LMB is basically a LIB in which the graphite ( $372 \text{ mAh g}^{-1}$  for  $\text{LiC}_6$ ) have been replaced by Li-metal ( $3862 \text{ mAh g}^{-1}$ ). As mentioned, this replacement can double

<sup>3</sup>This is a huge number. If you had  $10^{19}$  electrons, you could give every human on Earth a billion electrons each, and still have a some left over.

<sup>4</sup>The only other element that comes close to Li is beryllium ( $2974 \text{ mAh g}^{-1}$ ). Beryllium, however, is very toxic, scarce on Earth, and can be radioactive, why it is of little interest in commercial batteries [26].

the energy density [2] and drastically increase the specific energy of the cell [8]. An example of a LMB cell is shown during discharging in Figure 2.2, with LCO as the other electrode for easy comparison with the LIB cell in Figure 2.1. The replacement of graphite with Li-metal mean two main things. First, as stated, the specific capacity of Li-metal is almost ten times higher than that of lithiated graphite ( $\text{LiC}_6$ ). Thus, more total capacity is achieved for the same electrode material. Secondly, the Li now needs to be stripped away from the Li-metal during discharging, and must then plate the surface (being deposited there) during charging. The deposition can lead to several problems if it is non-uniform.

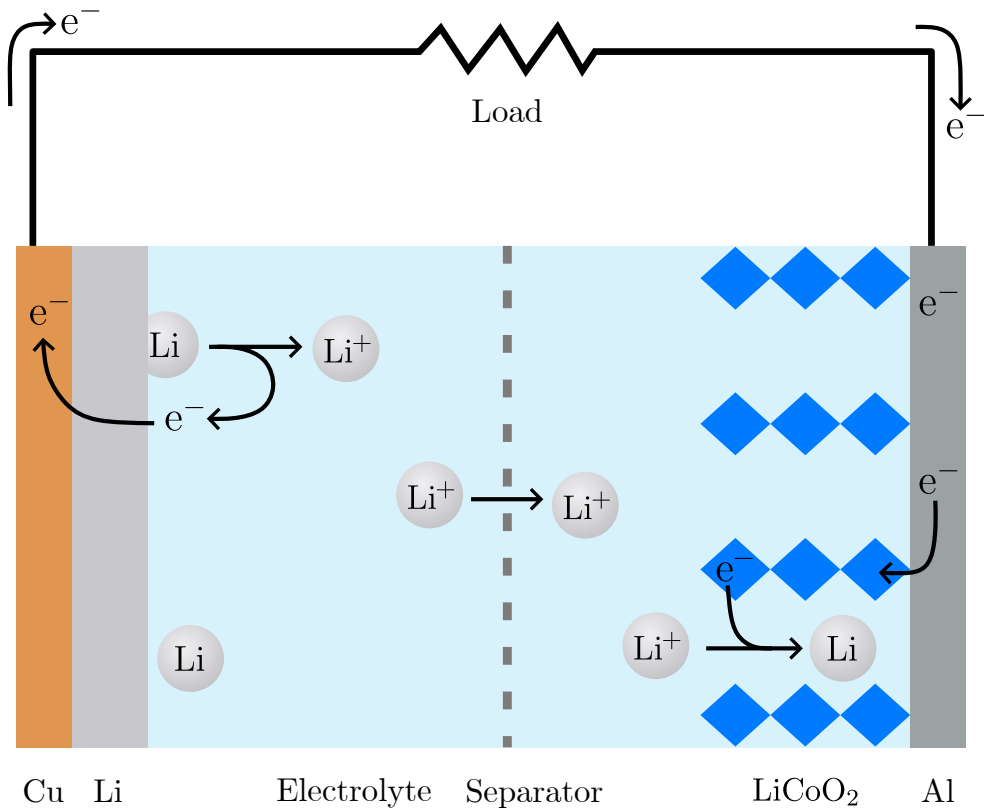


**Figure 2.2.** A schematic view of a cell in a LMB, showing the parts (not to scale) inside the cell casing during discharging. The parts are the same as in the case with the LIB cell (see Figure 2.1), with the graphite having been replaced by Li.

### 2.3.1 Problems with non-uniform lithium deposition

The deposition of Li on the Li-metal surface can cause several problems, as shown in Figure 2.3. First, the growing Li can penetrate the separator (not shown) and

come into contact with the opposite electrode, in this example the LCO, causing a short-circuit in the cell. This is a serious safety risk as short-circuiting can lead to thermal runaway which can end in catastrophic failure where the cell explodes [27]. Secondly, "dead" Li can form. The cell potential during deposition is outside the range for which the electrolyte is stable, causing the electrolyte to react with fresh Li in irreversible reactions and forming a solid electrolyte interphase (SEI) layer. This SEI layer is electronically isolating and generally wanted on the electrode surface, as it passivates the surface and thus reduces unwanted side reactions. However, when newly deposited Li comes into contact with the electrolyte, new SEI forms that can envelop a piece of Li, and possibly making it lose contact with the Li-metal electrode. The electronically isolated piece of Li is called "dead" Li. Creation of dead Li decreases the Coulombic efficiency<sup>5</sup> [27]. Thirdly, the non-uniform deposited Li is porous, as opposed to closely packed like the pristine Li-metal, leading to a significant change in volume of the electrode material. During many cycles, this repeated and large increase and decrease in volume builds up mechanical stress which can cause the SEI to crack and re-form (consuming more Li) [17]. Fourthly, since non-uniform growth of Li also increases the surface area exposed to the electrolyte, more (irreversible) side reactions occur between the Li and electrolyte. Amongst other things, this creates more overall SEI, decreasing the available Li for cycling and lowering the Coulombic efficiency [27]. All loss of active Li also leads to a decrease in the overall cell capacity.

As we have seen, there are several problems originating from non-uniform plating of Li that directly affects the cell performance through lowered Coulombic efficiency and loss of capacity over time. Finding ways to enable more uniform plating would eliminate, or at least lessen, these issues, thus improving the cell performance. To be able to reliably induce more favorable plating in LMBs, the first step during the deposition – nucleation – must first be well understood.

---

<sup>5</sup>Coulombic efficiency is defined as the ratio of charge extracted out of a battery during discharge divided by the charge inserted into the battery during charging. A low Coulombic efficiency means that charge is lost during cycling, leading to a shorter cycle life.

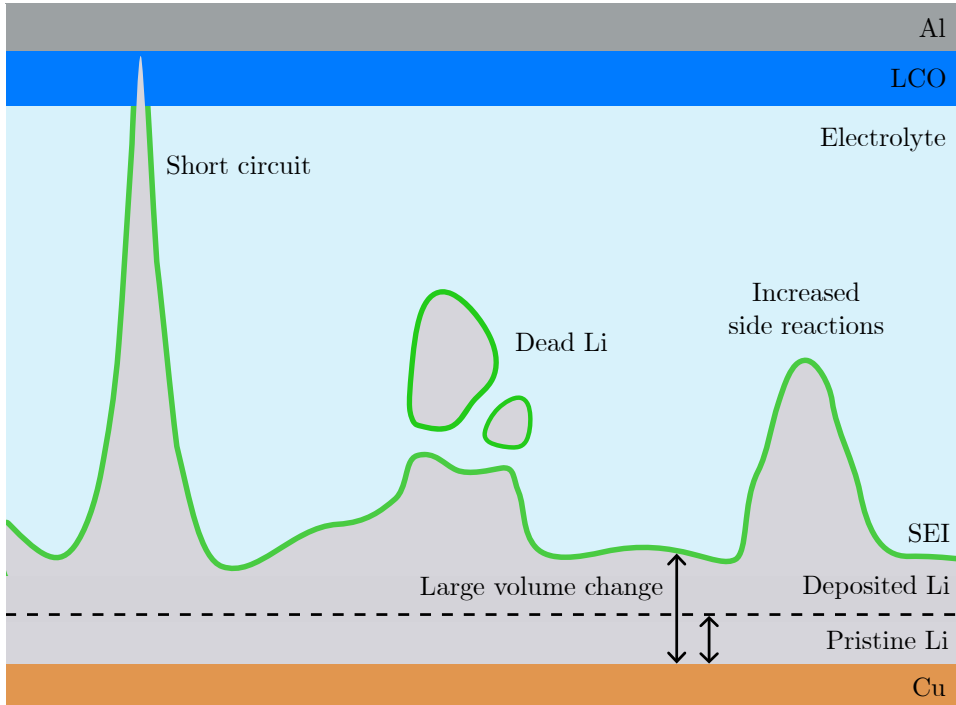


**Figure 2.3.** A schematic view of problems arising from non-uniform deposition of Li onto a pristine Li-metal surface in a LMB cell (not to scale). The main problems are short-circuiting the cell, formation of dead (electronically isolated) Li, large volume change, and increased rate of unfavorable side reactions. Short circuit occurs when the deposited Li penetrates the opposite electrode, here LCO. Dead Li is formed when a piece of Li becomes covered in a SEI layer (green outline around the deposited Li) and is therefore electronically isolated. Large volume change happens due to the deposited Li being more porous than the pristine Li. Increased side reactions arises from the increased surface area from the non-uniform deposited Li, providing more sites for side reactions. Figure inspired by [27].

# 3

## Nucleation

A key concept in this work is nucleation. Nucleation is the first step in forming a new phase or structure, which in this work means forming solid Li from a solution containing Li-ions. After having formed Li nuclei with a size large enough to be thermodynamically stable, the nuclei will continue to grow if supplied with more Li. In this section, the steps of nucleation are first described, followed by homogenous nucleation theory that provides important concepts for understanding nucleation. Lastly, the specific scientific questions this work aims to answer are presented.

### 3.1 Steps during nucleation and growth

Here we consider nucleation of Li from an electrolyte containing  $\text{Li}^+$  onto a Cu surface. Nucleation consists of several steps, shown in Figure 3.1. Following one (solvated) Li-ion, the first step is mass transport of the ion through the electrolyte and SEI layer (not shown) to the Cu surface. Next is charge transfer, where the Li-ion is reduced (gains an electron) and becomes a Li atom which can adsorb to the surface. Finally, the adsorbed Li combine into a cluster with other Li atoms and forms a nucleus. Growth of this formed nucleus occur in the same way, where additional Li-ions are reduced and adsorbed to the existing nucleus. For nucleation to occur, an energy barrier needs to be overcome. The presence of this energy barrier can be observed in a deposition curve.

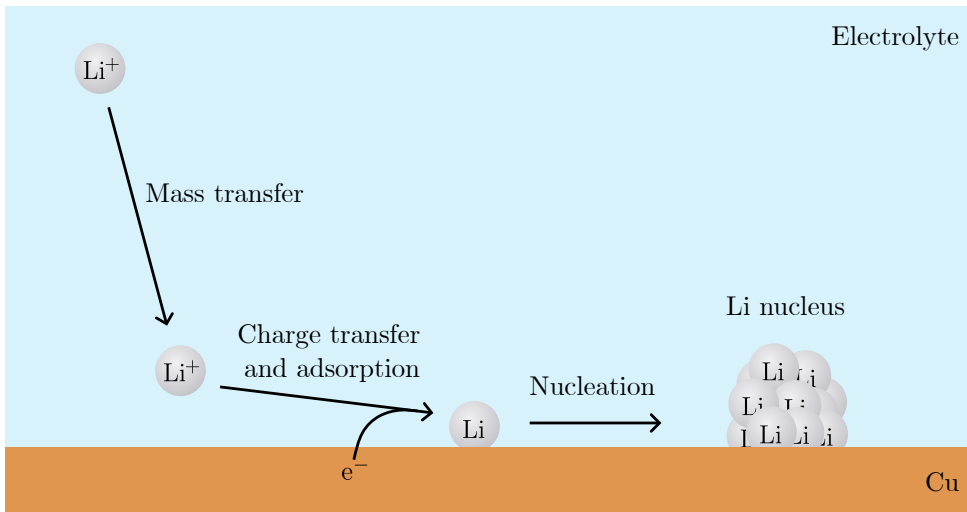


**Figure 3.1.** Steps during nucleation of Li. A  $\text{Li}^+$  gets transported through the electrolyte towards the Cu substrate. Then, an electron reduces the ion to a Li atom, which then adsorbs onto the surface. Nucleation occurs when many Li atoms cluster together, forming a nucleus. Figure inspired by [28].

## 3.2 Deposition curve in a lithium/copper cell

Here we consider deposition of Li in a cell with Li as one electrode material and Cu as the other. The characteristic deposition curve is shown in Figure 3.2 as the cell voltage as function of charge passed. A certain driving force, overpotential, is required to start the nucleation process on the bare Cu. This is seen as the sharp drop in potential, which reaches its lowest value at  $\eta_n$  (nucleation overpotential). At this region of the curve, nucleation occurs [29]. Once nuclei have formed, the voltage increases and reaches a plateau at  $\eta_p$  (plateau overpotential). At this region of the curve, nuclei grow [15]. Below the graph, a schematic illustration of Li deposition on the Cu surface is shown. The left-hand side shows that a voltage difference gives rise to an electric field, which exerts a force on positive charges like  $\text{Li}^+$  in the direction of the field lines. Li atoms from the Li electrode can be oxidized (release electrons) and move into the electrolyte as  $\text{Li}^+$ . The electric field drives mass transport of  $\text{Li}^+$  towards the Cu where the  $\text{Li}^+$  can be reduced (pick up electrons), forming Li nuclei by the steps presented in Figure 3.1. Hence, the charge passed through the outer circuit indicates the amount of deposited Li. Note that the overpotential for nucleation is larger in magnitude than the overpotential for growth,  $|\eta_n| > |\eta_p|$ . In other words, the energy barrier is different for nucleation and growth. This can be modelled theoretically with nucleation theory.

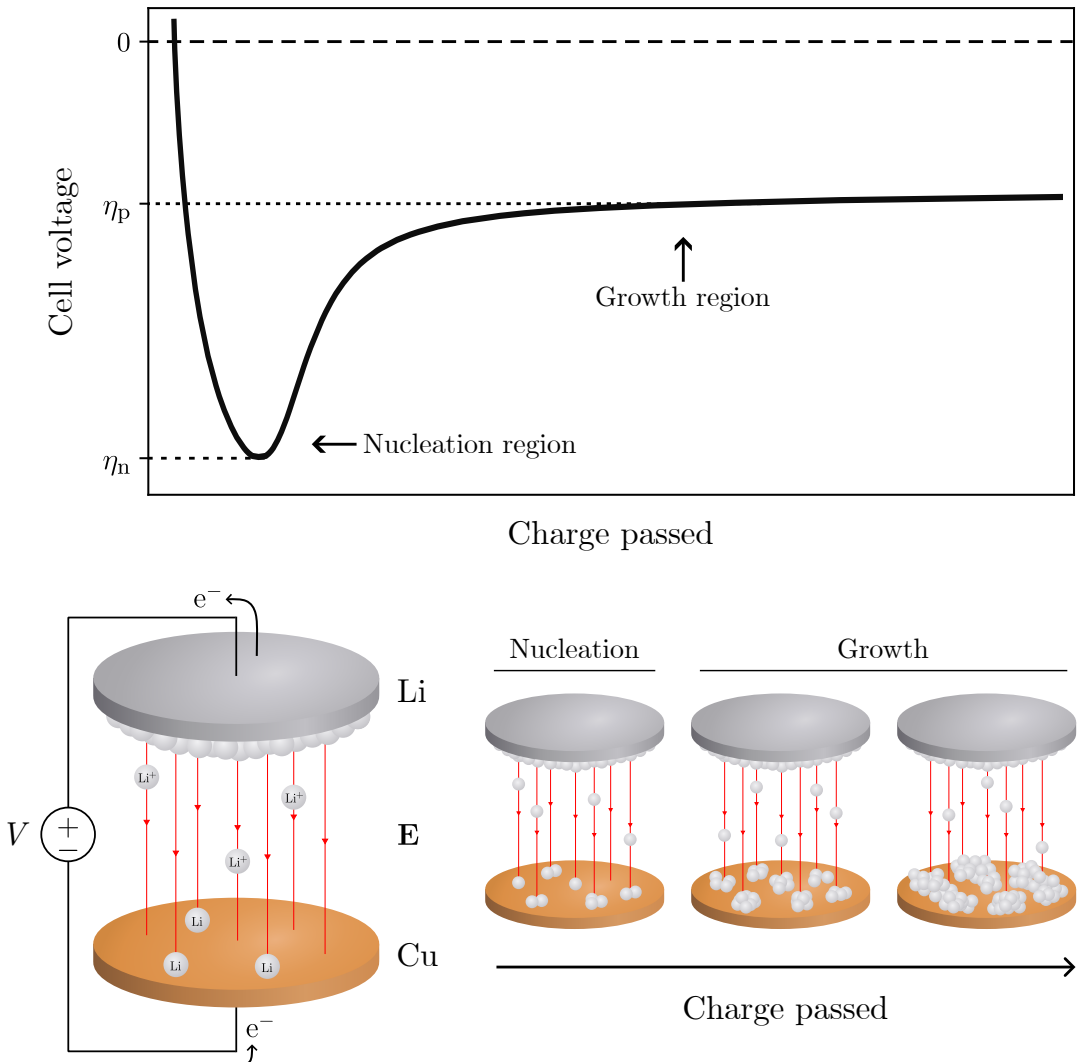


**Figure 3.2.** Top: Characteristic deposition curve showing cell voltage (versus Li) as function of charge passed. The overpotential for the nucleation region and for the growth (plateau) region,  $\eta_n$  and  $\eta_p$  respectively, are marked. Bottom: Illustration of Li deposition on Cu. A voltage difference  $V$  between the electrodes induces an electric field  $\mathbf{E}$  (red lines with arrows), exerting a force on positive charges like  $\text{Li}^+$  in the direction of the field lines. The  $\mathbf{E}$  drives  $\text{Li}^+$  toward the Cu, where the ions can recombine with electrons and form Li atoms on the surface. The deposited Li atoms first form nuclei (nucleation region), which then grow as more charge get passed (growth region).

### 3.3 Homogenous nucleation theory

Nucleation theory starts with thermodynamics, specifically the change in Gibbs free energy. In general terms, when a new solid phase is formed from a solution, there is a cost in energy for creating surface area ( $\Delta G_{\text{surface}} > 0$ ) and at the same time a gain in energy for creating bulk ( $\Delta G_{\text{bulk}} < 0$ ). In the case of homogenous nucleation, the change in Gibbs free energy for forming a nucleus can be written

$$\begin{aligned}\Delta G &= \Delta G_{\text{surface}} + \Delta G_{\text{bulk}} \\ &= A\gamma + V\Delta G_V \\ &= 4\pi r^2\gamma + \frac{4}{3}\pi r^3\Delta G_V\end{aligned}\tag{3.1}$$

where  $A$  is the surface area created,  $\gamma$  is the surface energy of the interface between the two phases,  $V$  is the volume of the nucleus,  $\Delta G_V$  is the change in Gibbs energy per created volume, and in the last line we assume that the nucleus is spherical with radius  $r$ . The overpotential  $\eta = \eta_n$  for nucleation is related to  $\Delta G_V$  as

$$\Delta G_V = -\frac{F|\eta|}{V_m}\tag{3.2}$$

where  $F$  is Faraday's constant and  $V_m$  is the molar volume of the element creating the nucleus [15]. The expression in Equation 3.1 is shown in Figure 3.3 as function of  $r$ . It is the cost in energy associated with  $\Delta G_{\text{surface}}$  that gives rise to the energy barrier  $\Delta G_{\text{barrier}} = \Delta G(r_{\text{critical}})$  for nucleation. Here,  $r_{\text{critical}}$  is the critical radius of nucleation, the radius for which the nucleus becomes thermodynamically stable. As long as the size of the nucleus is  $r < r_{\text{critical}}$ , it is unstable since the system could gain energy by taking away particles from it. But once  $r > r_{\text{critical}}$ , the nucleus grows spontaneously since this lowers the Gibbs free energy of the system. This can be shown by considering the change in Gibbs free energy for the addition of one particle to the nucleus. Adding one particle means a small increase  $dr$  to the radius and Gibbs free energy changes as  $\Delta G_{\text{particle}} = \Delta G(r + dr) - \Delta G(r)$ . If  $\Delta G_{\text{particle}} < 0$ , the Gibbs free energy is lowered and the nucleus grows spontaneously. Thus, the condition  $\Delta G(r + dr) < \Delta G(r)$  determines  $r_{\text{critical}}$ , which can be derived by setting the derivative of Equation 3.1 equal to zero and solving for  $r = r_{\text{critical}}$ ,

$$\begin{aligned}\frac{\partial}{\partial r}\Delta G &= (8\pi r\gamma + 4\pi r^2\Delta G_V) \Big|_{r=r_{\text{critical}}} \\ &= 8\pi r_{\text{critical}}\gamma + 4\pi r_{\text{critical}}^2\Delta G_V \\ &= 4\pi r_{\text{critical}}(2\gamma + r_{\text{critical}}\Delta G_V) \stackrel{!}{=} 0\end{aligned}$$

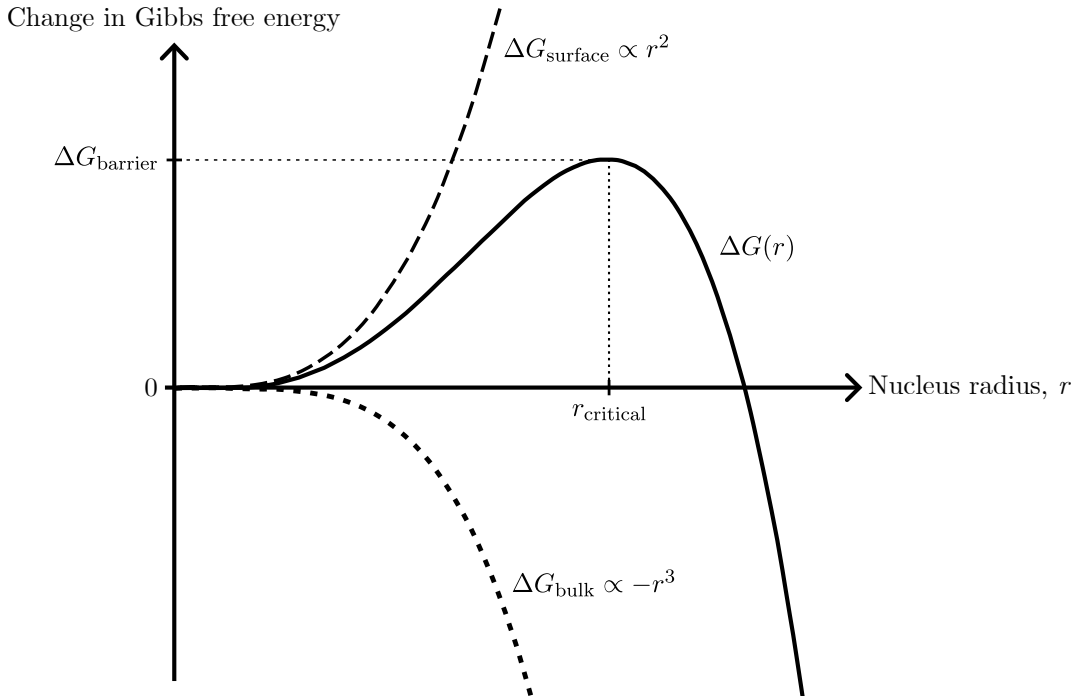


**Figure 3.3.** Characteristic plot of  $\Delta G(r) = \Delta G_{\text{surface}} + \Delta G_{\text{bulk}}$ , where  $\Delta G_{\text{surface}} \propto r^2$  and  $\Delta G_{\text{bulk}} \propto -r^3$  for a spherical nucleus. At the point where growth of the nucleus lowers the overall energy of the system, when  $\Delta G(r + dr) < \Delta G(r)$ , a critical radius  $r_{\text{critical}}$  is reached. Once  $r > r_{\text{critical}}$ , the nucleus grows spontaneously since this lowers the Gibbs free energy of the system. The energy cost for the surface induces an energy barrier  $\Delta G_{\text{barrier}} = \Delta G(r_{\text{critical}})$  that needs to be overcome for nucleation to occur.

which, ignoring the solution  $r_{\text{critical}} = 0$ , gives

$$r_{\text{critical}} = -\frac{2\gamma}{\Delta G_V}.$$

By using Equation 3.2 this results in

$$r_{\text{critical}} = \frac{2\gamma V_m}{F|\eta|} \quad (3.3)$$

from which we see that the size of the nuclei is inversely proportional to the overpotential,  $r_{\text{critical}} \propto \eta^{-1}$ . Moreover, given the same amount of deposited Li, one should expect not only that the size is dependent on  $\eta$  but also the number of nuclei per area. One can in fact show<sup>1</sup> that the areal nuclei density  $N$  is proportional to

<sup>1</sup>Given that  $r \propto \eta^{-1}$ , we can show that the areal nuclei density is proportional to the third power of the overpotential,  $N \propto \eta^3$ . First, let  $n$  be the number of nuclei,  $V$  be the total deposited

the overpotential to the third power,  $N \propto \eta^3$ . These relations,  $r_{\text{critical}} \propto \eta^{-1}$  and  $N \propto \eta^3$ , influence the nuclei distribution as function of overpotential, as shown in Figure 3.4. These theoretical relations have been supported by experiment [15].

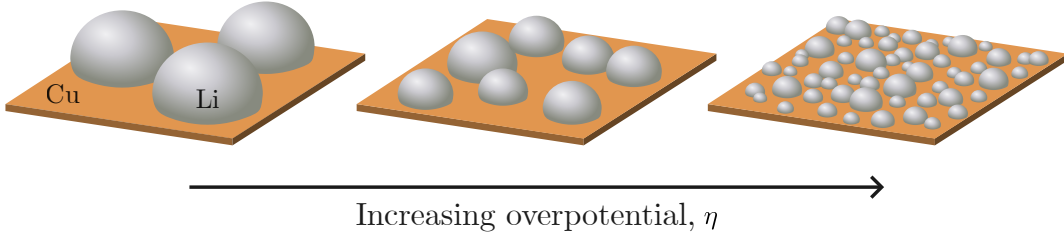


**Figure 3.4.** When the overpotential increases, the size of the Li nuclei decreases as  $r_{\text{critical}} \propto \eta^{-1}$  while the areal density increases as  $N \propto \eta^3$ . Figure inspired by [15].

The presence of a substrate means that it is heterogeneous, and not homogenous, nucleation which actually takes place. While heterogeneous nucleation theory can model nucleation on a flat surface by taking more parameters into account, the case of homogenous nucleation already provides the most essential concepts needed to understand nucleation. We have seen that it is the cost in energy for creating surface area, as opposed to the gain in energy for creating bulk, which leads to an energy barrier for nucleation. This can be seen in the deposition curve (Figure 3.2), where a large  $|\eta_n|$  is required for nucleation, but a smaller  $|\eta_p|$  is sufficient for subsequent growth. This is explained as the surface term in  $\Delta G$  scaling as  $r^2$ , while the bulk term scales as  $-r^3$ . Furthermore, the overpotential influences both the size and areal density of the nuclei, following  $r_{\text{critical}} \propto \eta^{-1}$  and  $N \propto \eta^3$ . Having provided a fundamental understanding of the nucleation process through nucleation theory, the scientific questions addressed in this work will now be presented.

## 3.4 Scientific questions addressed in this work

As previously stated, this work will investigate the nucleation of Li by using electron microscopy to image deposited Li, and by performing electrochemical measurements. First, the necessary experimental procedures to obtain clean electron

---

volume,  $r$  be the radius of the nuclei, and  $A$  be a fixed area on which  $N$  is calculated. Next, we have  $V = nr^3$  because the total volume deposited is the number of nuclei times their volume (assuming spherical nuclei), which gives  $n = V/r^3$ . Since we seek  $N = n/A$ , we put together the relations above to get  $N \propto n \propto r^{-3} \propto \eta^3$ , where  $r \propto \eta^{-1}$  was used in the final step. Finally, we arrive at the conclusion that  $N \propto \eta^3$ , in agreement with [15].

---

### 3.4. Scientific questions addressed in this work

microscope images of deposited Li will be investigated. Then, the main focus of this work will be on how the nucleation process is influenced by 1) the degree of passivation of the Cu surface before deposition, 2) the deposition current density, and 3) the pressure between the Li and Cu. In particular, the size and distribution of nuclei will be examined with respect to the pressure, while the shape of the deposition curve is of interest regarding the degree of passivation, the current density, and the cell configuration. Also, the influence of different electrolytes will be tested.



# 4

## Methods

This section first shows the material preparation and the different types of cell configurations used. Then, the setup and protocols used for electrochemical cycling of the cells are described, followed by a section focusing on the scanning electron microscope (SEM). Lastly, the data analysis of the obtained SEM images and cycling data is explained.

### 4.1 Material preparation

#### 4.1.1 Electrode materials

The electrode materials used were Cu (Goodfellow, 0.1 mm thick sheet, 99.9 % purity) and Li (Chemetall, 0.2 mm thick). The Li was prepared inside the argon-filled glove box by punching out circular pieces with a diameter of 5 mm, while the preparation of Cu took place outside the glove box. Preparation began with polishing, where each Cu sheet was polished using grinding paper placed on a turn table (Buehler Beta grinder-polisher), see Appendix A.1 for details. This resulted in a mirror-like finish for the Cu sheet. As shown in Figure 4.1, a puncher was used to produce circular disks of Cu with diameter 10 mm from the polished sheet. Next followed the washing procedure of the circular disks. A ultrasonic cleaner (Fisherbrand Easy) was used, where each Cu piece was placed polished side up in its own glass beaker to avoid scratches during the washing procedure. Each glass beaker containing one Cu piece was filled with acetone and put into the ultrasound cleaner for 10 min at room temperature. The acetone was thereafter poured out, and each glass beaker filled with isopropanol for another ultrasound clean for 10 min at room temperature. The Cu disks were then dried by pouring

out the solvent and letting the remaining solvent evaporate, after which the disks were placed in a glass beaker and finally transferred into the glove box.

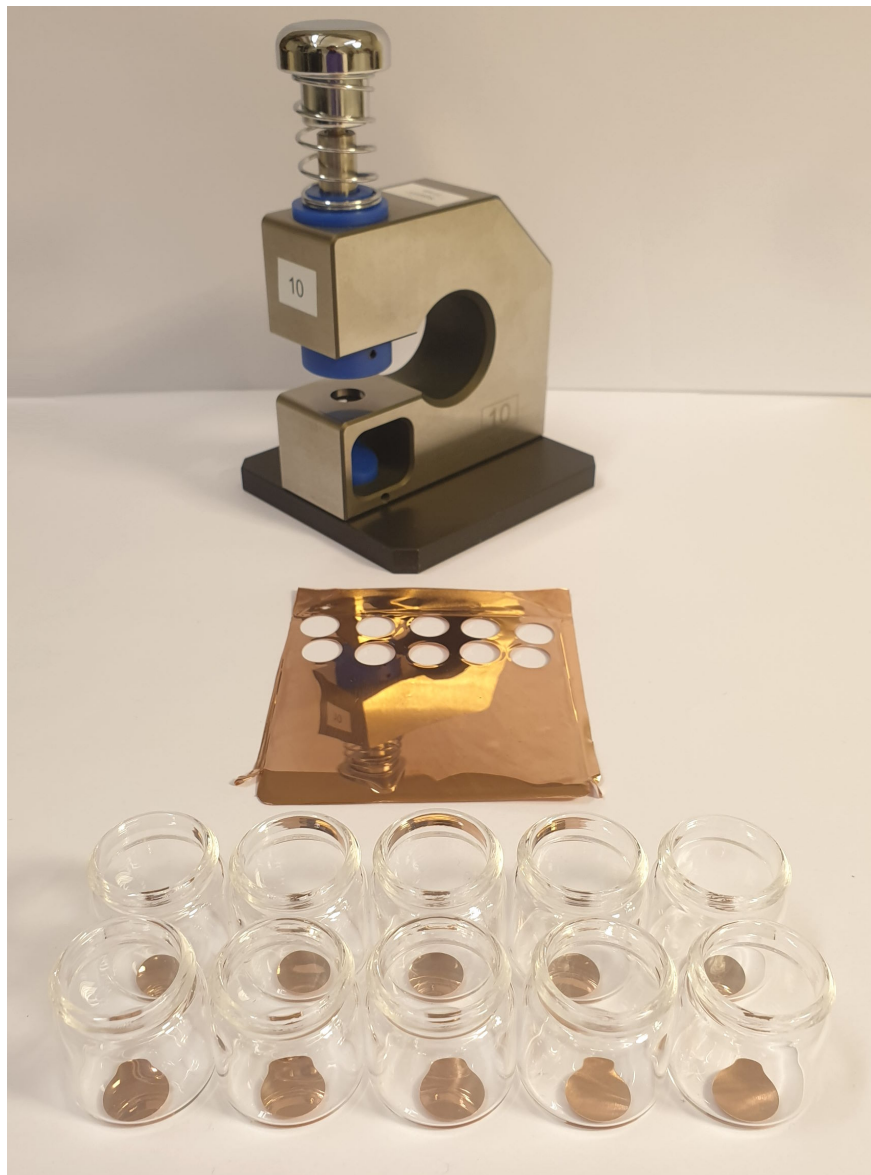


**Figure 4.1.** The puncher was used to punch circular disks with diameter 10 mm out of the polished Cu sheet. One 70 mm × 70 mm sheet resulted in about 30 Cu disks.

### 4.1.2 Electrolytes

The main electrolyte used was lithium bis(fluorosulfonyl)imide (LiFSI) salt in the solvent 1,2-dimethoxyethane (DME). The LiFSI salt was dried in an oven (Büchi

B-580) at 80 °C for at least 24 h under vacuum. To remove water molecules from the solvent, the DME was put into a glass vial together with molecular sieves with pore size 3 Å. The molecular sieves had previously been dried in the oven at 230 °C for 24 h under vacuum. The DME soaked the molecular sieves for at least 24 h and the DME was then pushed through a filter to remove any impurities from the molecular sieves (Acrodisc PSF with 0.45 µm pore size) before use.

The main electrolyte had a 4 mol L<sup>-1</sup> concentration of LiFSI salt in DME. This concentration was achieved by using a mole ratio of 1.4/1 (DME/LiFSI) [12]. The two other electrolytes used were lithium hexafluorophosphate (LiPF<sub>6</sub>) and an ionic liquid (IL). The LiPF<sub>6</sub> consisted of 1.0 mol L<sup>-1</sup> LiPF<sub>6</sub> salt in ethylene carbonate (EC) and ethyl methyl carbonate (EMC) with volume ratio 1/1 (EC/EMC). The LiPF<sub>6</sub> electrolyte was used as received from Sigma-Aldrich. The IL consisted of lithium bis(trifluoromethanesulfonyl)imide (LiTFSI) in the electrolyte 1-Butyl-1-methylpyrrolidinium bis(fluorosulfonyl)imide (Pyr<sub>14</sub>FSI) with mole ratio 1/4 (LiTFSI/Pyr<sub>14</sub>FSI). The LiTFSI had been dried at 80° for 24 h in vacuum. Both the LiTFSI and the Pyr<sub>14</sub>FSI were bought from Solvionic. Preparation of the electrolytes and the DME was carried out in a glove box filled with argon gas.

## 4.2 Cell configurations and assembly

The cell configuration includes the geometry, choice and volume of electrolyte, choice of separator, and pressure between the electrodes. Described below are the configuration and assembly of the coin cell (C-cell), the Swagelok-type two-electrode cell (I-cell), and Swagelok-type three-electrode cell (T-cell). The C-cell is a common configuration, although the pressure between the electrodes can be unevenly distributed [30]. On the other hand, the I-cell can be built with a hopefully more even pressure between the electrodes. Lastly, the T-cell can be built without pressure between the electrodes and also enables measurement with a reference electrode. All cells were assembled inside an argon-filled glove box with oxygen levels below 4 ppm and water levels below 0.01 ppm.

### 4.2.1 The coin cell (C-cell)

Figure 4.2 shows the parts that make up a C-cell and the assembly. The main parts of the cell are Li, separator and electrolyte, and Cu. The can, gasket, and cap keep the main parts in place and seals the cell shut, while the wave spring applies pressure between the electrodes. For each cell, Wellcos 2032 type cell parts were used and 25  $\mu\text{L}$  of electrolyte was added to one separator using a micropipette during assembly. Specifically, most C-cells were assembled with 25  $\mu\text{L}$  electrolyte of  $4 \text{ mol L}^{-1}$  LiFSI in DME added to one Celgard 2400 separator. However, when comparing electrolytes one cell instead had 25  $\mu\text{L}$  electrolyte of  $1 \text{ mol L}^{-1}$  of LiPF<sub>6</sub> in 1/1 volume ratio of EC/EMC added to one Celgard 2400 separator, and one cell had 25  $\mu\text{L}$  of the IL added to one Whatman glass microfiber filter separator grade GF/C (because the IL did not wet the Celgard 2400 separator).

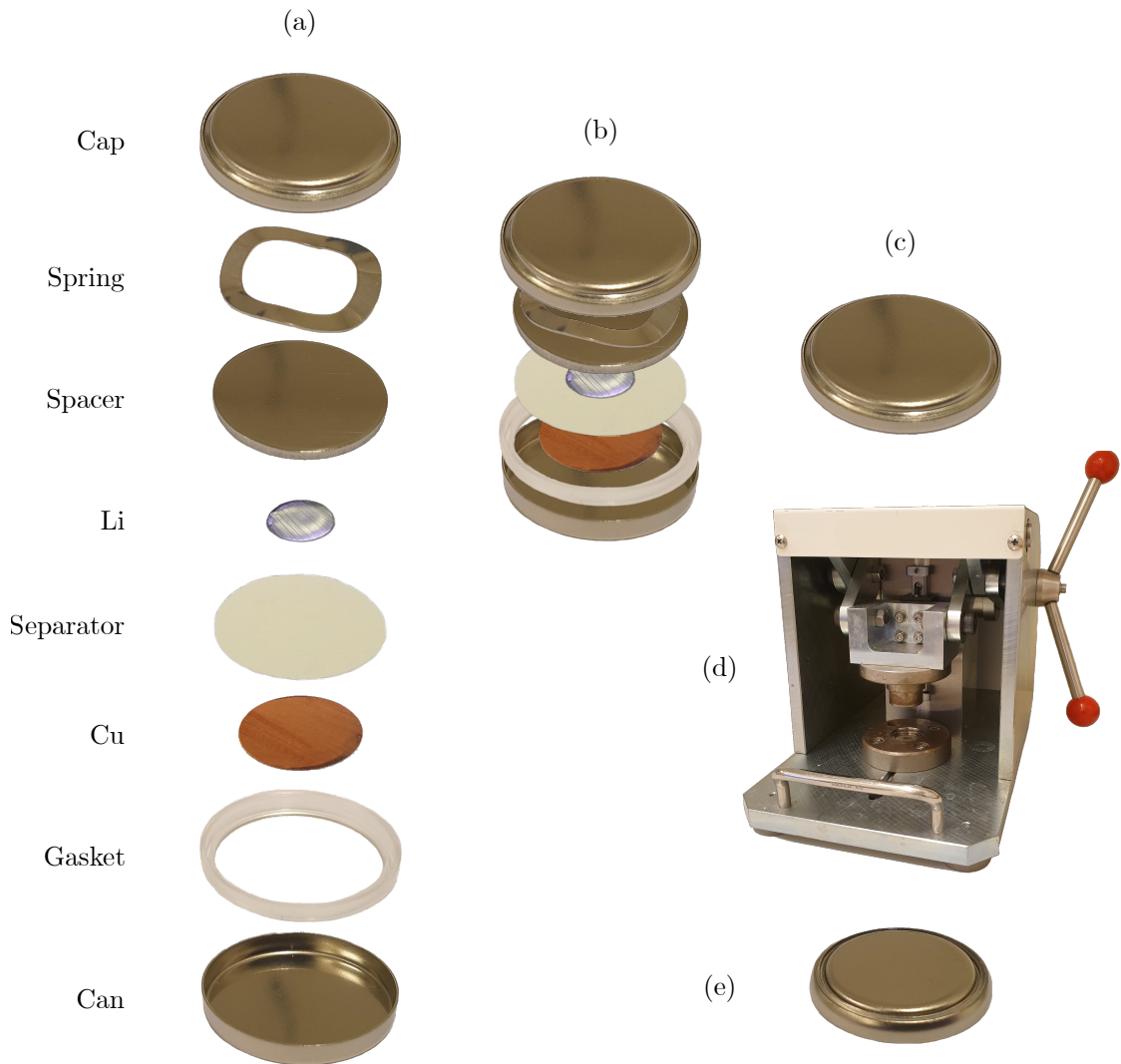


**Figure 4.2.** (a) The parts of the C-cell with Li and Cu. Electrolyte is added to the separator during assembly, and (b) the parts are first put into the can as shown, and the cap is first pushed into the gasket by hand, resulting in (c). The assembly is then finalized by bending the can walls inwards using (d) a hand-turned press (not to scale), ensuring a tight fit between the can, gasket, and cap, resulting in (e) the assembled and closed C-cell.

### 4.2.2 The Swagelok two-electrode cell (I-cell)

This cell is a Swagelok-type<sup>1</sup> two-electrode cell, as it has two electrodes which in this case are metal rods connecting to the Li and Cu. The parts and assembly process of the I-cell are shown and described in Figure 4.3. Though most of the parts are stainless-steel, the metal rods are physically separated from the main body by virtue of the non-conductive Swagelok sealing rings, preventing a short circuit between the Li and Cu. For each cell, 25  $\mu\text{L}$  electrolyte of 4 mol L<sup>-1</sup> LiFSI in DME was added to one Celgard 2400 separator using a micropipette during assembly.

To apply pressure between the Li and Cu, a spring was used. The pressure was calculated by measuring the total length of each assembled I-cell (from which the compression length of the spring could be computed), and taking the area of interest to be that of the punched Li 5 mm in diameter. This resulted in a pressure equal to  $(267 \pm 16)$  kPa, or  $(2.64 \pm 0.16)$  atm, for all assembled I-cells. The uncertainty in the pressure comes from error propagation of the quantities used to calculate the pressure, also taking into account different total lengths of the assembled cells.

---

<sup>1</sup>Swagelok refers to the way two conical plastic rings are used together in order to achieve a leak-tight seal, here between the steel rods and the walls of the cell (see Figure 4.3). The rings are called the front and back ferrule, and will together be referred to as Swagelok sealing rings for clarity.

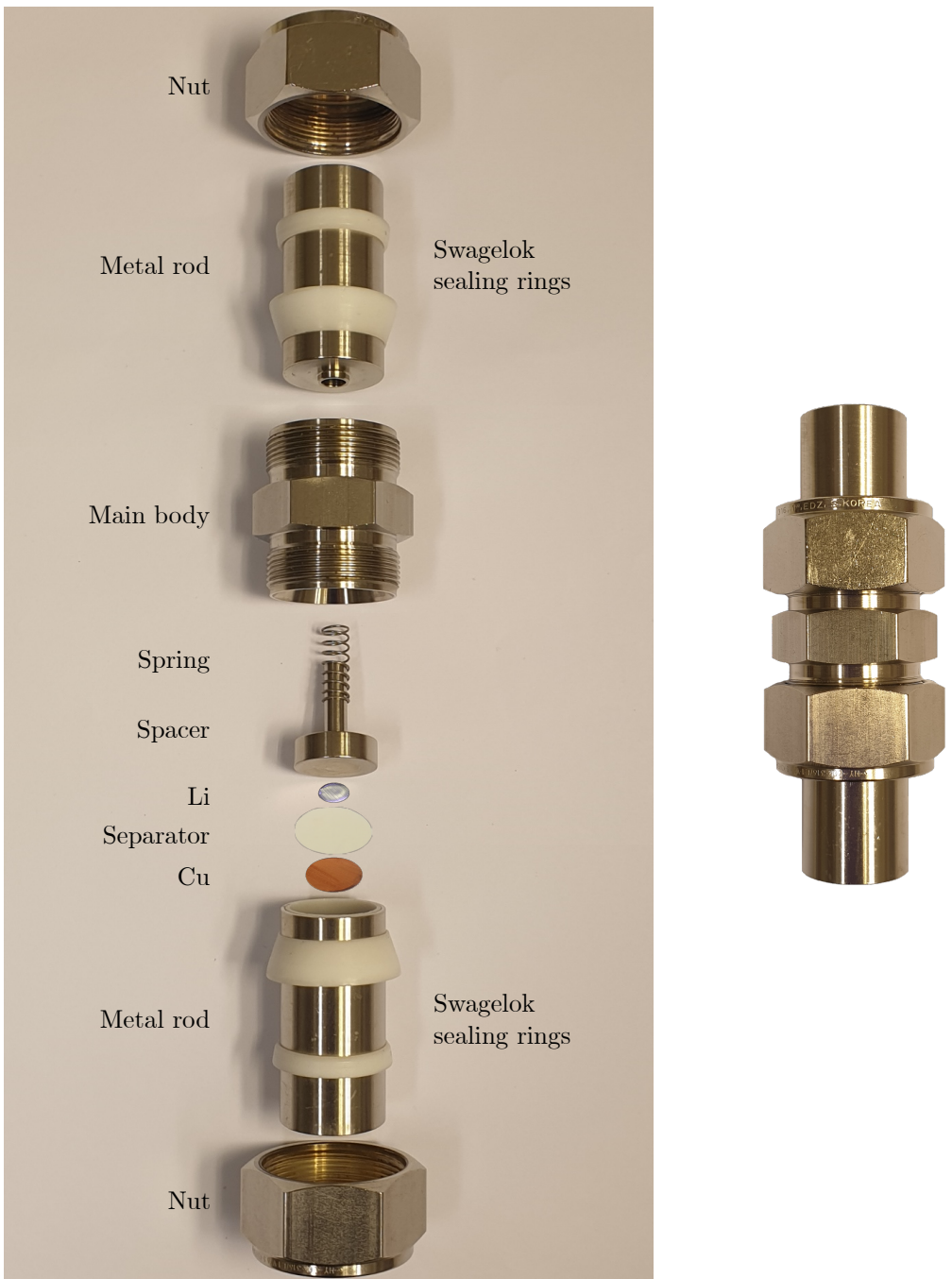


**Figure 4.3.** Parts of the I-cell. First, the Cu, separator, electrolyte (added to the separator during assembly), and Li are put into the lower metal rod in that order. The rest of the cell is then assembled by moving the other parts inwards and tightening the nuts onto the main body. Tightening of the nuts achieves a leak-tight seal thanks to the Swagelok sealing rings. The spring, being compressed during assembly, applies pressure to the Li and Cu. The assembled I-cell is shown to the right.

### 4.2.3 The Swagelok three-electrode cell (T-cell)

For a cell without pressure between the electrodes, the T-cell will be used. In this case, a custom-built Swagelok-type T-cell made of polyether ether ketone (a plastic with high chemical resistance) and stainless-steel rods was used. The main body of the cell has a hollow T-part, allowing three metal rods to be inserted. The parts of the T-cell are shown in Figure 4.4. The 1 mm polypropylene (PP) horseshoe-shaped spacer used was made from a 1 mm thick sheet of PP, see Appendix A.2 for details. The spacer prevents physical contact between the Li and Cu, meaning there is no applied pressure between the two electrodes. For each assembly, 75  $\mu\text{L}$  electrolyte of  $4 \text{ mol L}^{-1}$  LiFSI in DME was added using a micropipette (no separator was used).

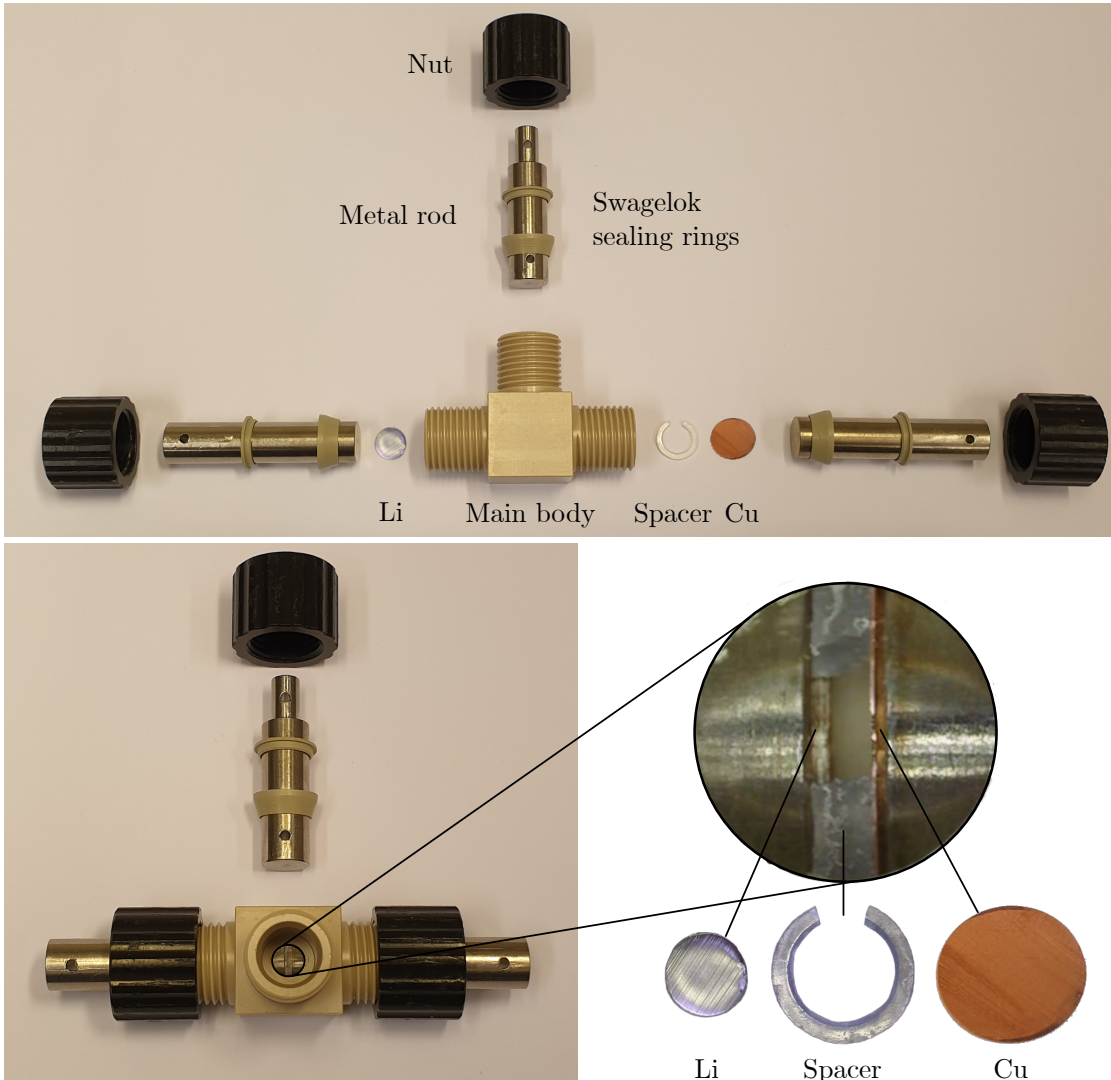


**Figure 4.4.** Parts of the T-cell. First, the metal rods on the sides are inserted along with the Li, spacer, and Cu. Then, the Swagelok sealing rings are mounted on the metal rods and the leak-tight seal is achieved by tightening the nuts onto the main body. Next, the electrolyte is added through the opening in the spacer, as shown in the magnification. The assembly is finalized by inserting the third metal rod and tightening the last nut. The magnification shows that the spacer creates a gap between the Li and the Cu, meaning there is no applied pressure between the electrodes.

## 4.3 Electrochemical cycling of the cells

Once a cell was assembled, it was attached to an instrument and subjected to a cycling protocol. For the samples to be measured in SEM, the Scribner Associates 580 Battery Test System was used for cycling of C-cells. For all other measurements, the VMP3 Multichannel Potentiostat (Biologic) was used. Moreover, the C-cells and I-cells were cycled outside the glove box at ambient conditions, while the T-cells were cycled inside the glove box. The cycling protocol is described below, as well as the sample preparation after cell disassembly for the measurements in SEM.

In general terms, the goal for the cycling protocol was to first see an indication that the cell had been assembled correctly, then to passivate the Cu surface, and finally to deposit Li on the Cu. These three steps are shown schematically in Figure 4.5. The first step, seeing that the cell was not obviously bad, was done by having a period when the open-circuit voltage (OCV) is measured. OCV is the potential of the cell when no load is connected to the cell. In the case of the Li/Cu cell, a good OCV means a cell potential of about  $(2.8 \pm 0.2)$  V.<sup>2</sup> The second step, to passivate the substrate, was achieved by forming the SEI by breakdown of the electrolyte through a constant voltage hold at low potential. When the voltage is held constant, the current is allowed to change freely. The current was therefore used as an indicator of how passivated the substrate was. When a low current is reached, the side reactions (such as forming the SEI) must occur slowly, and the substrate is thus more passivated. The third step, deposition of Li, was performed by applying a constant current in the direction such that Li is forced to move to the Cu. All in all, the cycling protocols were made up of three main parts, the OCV checking the cell status, followed by the constant voltage hold forming the SEI layer, and finally the constant current depositing Li.

### 4.3.1 Cycling protocol for SEM images

For the measurements in SEM, the cycling protocol was as follows. First 1 min of OCV, then 15 min of constant voltage at 0.010 V, and finally constant current deposition using  $J_{\text{deposition}} = 1 \text{ mA cm}^{-2}$  and various  $t_{\text{deposition}}$ . The length of  $t_{\text{deposition}}$  affects the total deposited areal capacity ( $\text{mAh cm}^{-2}$ ) for a given  $J_{\text{deposition}}$ .

---

<sup>2</sup>The convention here was to connect the cell to the instrument such that the OCV of the cell was positive.

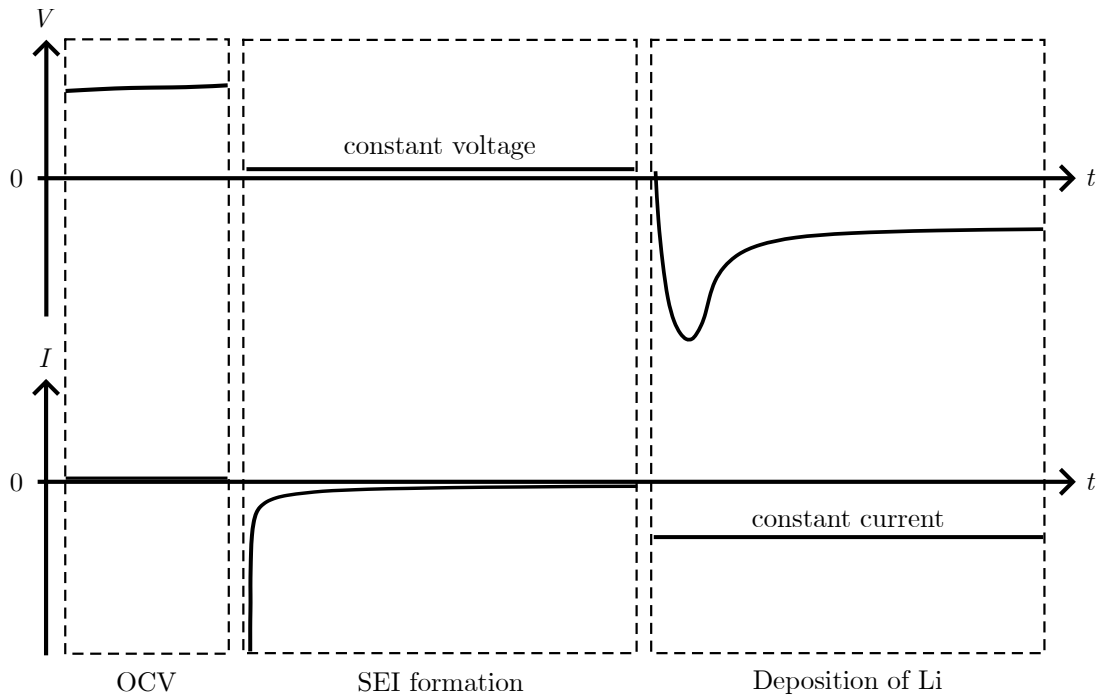


**Figure 4.5.** Schematic overview of the cell potential  $V$  and current  $I$  versus time  $t$  during the main three stages of the cycling protocol. The OCV measures the cell potential after assembly. Then follows a constant voltage hold at low potential to form the SEI layer. Here the current decreases fast at first, and then more slowly. Finally, deposition of Li takes place at constant current, resulting in the deposition curve.

### 4.3.2 Cycling protocol for electrochemical measurements

For the electrochemical measurements, the cycling protocol was as follows. First 1 min of OCV, then a constant voltage hold at 0.010 V until a cutoff value  $I_{\text{SEI-cutoff}}$  was reached, then a short OCV period for 0.1 s, and finally constant current deposition using  $J_{\text{deposition}}$  with a total deposited areal capacity of  $500 \mu\text{Ah cm}^{-2}$ . The purpose of the second OCV step was only to allow the software of the Biologic to change the current range during measurement when switching from the SEI formation (low current) to the Li deposition (in some cases much higher current). Optimally, the second OCV should not be present, although its short duration meant it is unlikely to have had any significant effect on the results.

When creating the cycling protocol in the Biologic software, the data acquisition could be controlled for the different parts of the protocol. Acquisition of a data point was made each time either the current or potential changes by some value,  $\Delta I_{\text{acquisition}}$  or  $\Delta E_{\text{acquisition}}$ , or some time had passed since the last acquisition,

$\Delta t_{\text{acquisition}}$ . During the OCV part,  $\Delta t_{\text{acquisition}} = 10$  s. For the SEI formation part,  $\Delta I_{\text{acquisition}} = 50 \mu\text{A}$  and  $\Delta t_{\text{acquisition}} = 10$  s. During this part of the protocol, the current range was set to automatic, meaning that the range of currents that the instrument could accurately measure automatically changed as the magnitude of the current during the SEI formation changed. For the part with deposition of Li,  $\Delta E_{\text{acquisition}} = 1$  mV and  $\Delta t_{\text{acquisition}} = 10$  s. The current range was in this part set to a value corresponding to  $I_{\text{deposition}}$ .

### 4.3.3 Sample preparation for SEM

For the samples to be measured in SEM, each cell was disassembled and the Cu washed inside the glove box. The washing procedure consisted of immersing and letting the Cu rest in fresh DME for 1 min. The Cu was then carefully touched edge on to a napkin in order to drain the DME from the surface. Next, the washed and dried Cu was attached by adhesive Cu tape to the SEM sample stage (a metal cylinder). Finally, the SEM sample stage was transported in an argon filled transfer chamber to the SEM instrument.

## 4.4 Electron microscopy

To image the nucleated Li, it is necessary to have sufficiently high resolution. Since optical microscope uses visible light to image objects, they can at best resolve two points about  $0.3 \mu\text{m}$  apart.<sup>3</sup> However, the resolution of an imaged object improves with shorter wavelength, and it is possible to reach shorter wavelengths by using electrons instead of visible photons.<sup>4</sup> That is the idea of an electron microscope, in which a spatial resolution of  $0.001 \mu\text{m}$  can be achieved [32]. An electron microscope is favorable in this study, as the size of deposited Li nuclei can be  $1 \mu\text{m}$  [15].

---

<sup>3</sup>The Abbe diffraction limit gives the spatial resolution of a microscope as  $r = \lambda / (2n \sin \theta)$  where  $r$  is the distance between two resolvable points (the resolution),  $\lambda$  is the wavelength of the particle used to image the object,  $n$  is the refractive index of the media surrounding the imaged object, and  $\theta$  is half the opening angle to the imaging lens [31]. Assuming  $n \sin \theta = 1$  for a lens in air, and using green light,  $\lambda = 500 \text{ nm}$ , one finds that  $r \approx 0.3 \mu\text{m}$ .

<sup>4</sup>Let us compare the wavelength of electrons and visible photons. Combining kinetic energy  $E_k = mv^2/2 = p^2/(2m)$ , where  $m$  is mass,  $v$  is speed, and  $p$  is momentum, with the de Broglie wavelength  $\lambda = h/p$ , where  $h$  is Planck's constant, we get  $\lambda = h / (2mE_k)^{1/2}$ . This gives that an electron accelerated to 10 keV has a wavelength of  $0.012 \text{ nm}$ . This is several orders of magnitudes lower than the wavelengths of visible photons between 400 nm and 700 nm.

#### 4.4.1 The scanning electron microscope (SEM)

The main components of a SEM are shown schematically in Figure 4.6. All parts of the SEM are enclosed in a vacuum chamber to avoid both contaminating the sample and having the electron beam deflected by other molecules. Starting from the top, the electron gun provides free electrons, for example by thermal emission of electrons from a heated tip of tungsten. A positively charged ring (the accelerator) then attracts and thereby accelerates the negatively charged electrons downwards in Figure 4.6, towards several electromagnetic lenses. The electromagnetic lenses generate magnetic fields (by passing current through coils of wire) which focuses the electrons to a fine beam with a small diameter. A small electron beam diameter means high spatial resolution. Electrons in the beam are called primary electrons and interact with the atoms in the sample, which can cause electrons to be emitted. Such electrons emitted from the sample are called secondary electrons and are measured using a secondary electron detector (SED). Closest to the sample are the so-called scanning coils. These coils deflect the electron beam sideways in a controlled manner, allowing the electron beam to be raster scanned across the surface of the sample. All the probed spots (pixels) during the raster scan come together to form a black and white image, where the intensity of each pixel is proportional to the signal from the SED (white means high signal and black means low signal). Images were obtained using a SEM (PHI 700 scanning Auger nanoprobe) with an acceleration voltage of 10 kV and a beam current of 10 nA for the C-cell samples and 5 nA for the T-cell samples.

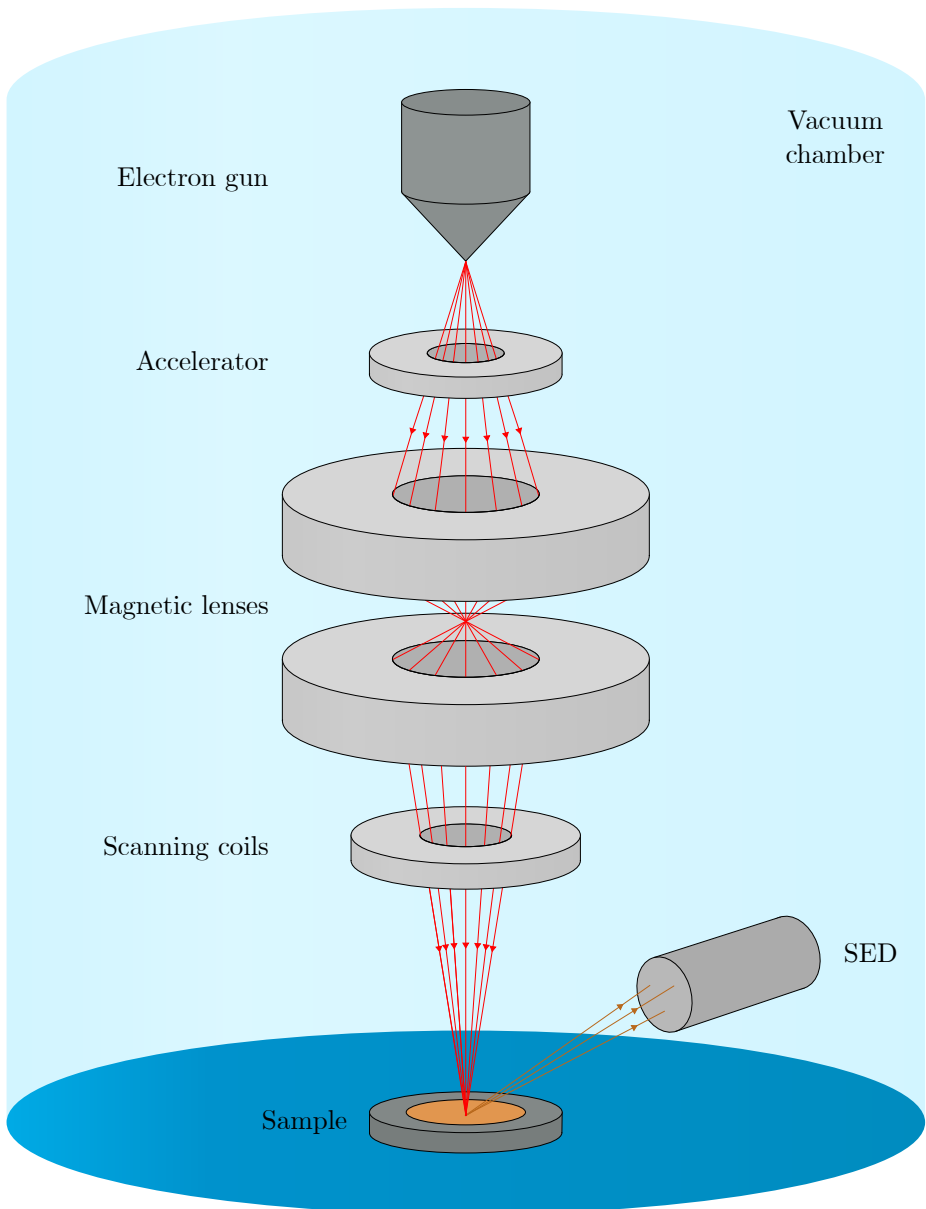


**Figure 4.6.** Schematic overview of the main components of a SEM. The electron gun ejects electrons (whose trajectories are represented as solid red lines) that get accelerated by the accelerator. The electrons are then focused to a small point by the magnetic lenses. The scanning coils raster scans the beam over the sample, resulting in ejected electrons that are finally measured using detectors, for example using a secondary electron detector (SED). The final imaged is obtained through software where a pixel image is build up from the detector signal during the raster scan.

## 4.5 Data analysis

The SEM images were obtained as grayscale  $512\text{ px} \times 512\text{ px}$  images. The nuclei areal density  $N$  (number of nuclei per area) and the typical diameter  $2r$  of the nuclei were obtained for a few selected images. For the nuclei areal density, the number of particles were counted manually and divided by the total area of the imaged surface. The typical diameter of the nuclei were also obtained manually, by comparing about 50 nuclei in each image to the scale bar which were divided into segments of  $1\text{ }\mu\text{m}$  during comparison.

The main quantities measured during the electrochemical cycling were time, cell potential, and current. The time was shifted such that the data for each cell began on zero when the SEI formation started. For the Li deposition, the charge passed (per electrode area) was calculated. Charge passed ( $\text{mAh cm}^{-2}$ ) is in this context defined as the deposition current (mA) divided by the Li area ( $\text{cm}^{-2}$ ) integrated with respect to time (h) during the deposition step. Plotting the deposition as cell potential versus the charge passed, instead of versus time, makes comparison of the curves easier for different  $J_{\text{deposition}}$ .



# 5

## Results and discussion

The main questions of this work are how the degree of passivation of the Cu surface and the deposition current density influences the shape of the deposition curve, and how the pressure between the Li and Cu electrodes impacts the size and distribution of deposited Li nuclei. Also, there are questions of what procedures are necessary to obtain SEM images with a clear view of the Li nuclei, and what effect the electrolyte has on the deposition curve.

### 5.1 Passivation of the Cu surface before deposition

Different reactions can occur at the start of the deposition, including formation of the SEI layer, other parasitic reactions, and the deposition of Li. Therefore, it is interesting to see how these side reactions, all reactions which are not deposition of Li, influence the deposition curve. To this end, the dimensionless variable  $\sigma$  is introduced. Here,  $\sigma = I_{\text{SEI-cutoff}}/I_{\text{deposition}}$ , where  $I_{\text{SEI-cutoff}}$  is the value (ignoring the sign) that when reached during the SEI formation will stop the constant voltage hold and start the constant current deposition of Li at current  $I_{\text{deposition}}$  (ignoring the sign). Thus,  $\sigma$  represents what fraction of the deposition current drives side reactions at the very start of the deposition of Li. Because different cell configurations have different sized areas covered by the electrolyte, the parameter  $\sigma$  was used in an effort to fairly compare the deposition curves. To investigate the influence of  $\sigma$  on the deposition curve, T-cells and C-cells were built and cycled with different values of  $\sigma$ .

The top part of Figure 5.1 shows the current in a T-cell as function of time during the SEI formation by holding a constant cell potential of 0.010 V, while the bottom

part shows the subsequent deposition curves for the different values of  $\sigma$ . During the SEI formation, reactions occur that passivates the Cu surface, decreasing the current fast at first and then more slowly. The time taken to reach smaller values of  $\sigma$  in a T-cell increase rapidly, requiring 1.7 min to reach  $\sigma = 0.50$  and 2.0 h to reach  $\sigma = 0.05$ , but 16 h for  $\sigma = 0.02$  and over 25 h to go below  $\sigma = 0.01$  (all in the case of  $J_{\text{deposition}} = 1 \text{ mA cm}^{-2}$ ). As the current reached  $I_{\text{SEI-cutoff}}$  for each respective  $\sigma$ , deposition then took place which is shown as cell potential as function of charge passed. For large  $\sigma$ , the current from side reactions are large enough to prevent obvious nucleation. In other words, the side reactions are at the beginning enough to drive the current without the necessity of Li deposition. However, for larger values of charge passed, the deposition curves reach more or less the same cell potential (see Figure B.3 in Appendix B.2). For sufficiently small currents of the side reactions ( $\sigma \leq 0.50$ ), deposition of Li becomes necessary to supply the current, and the nucleation peak presents itself. It is evident that the choice of  $\sigma$  affect the shape of the deposition curve, where smaller values of  $\sigma$  means a more pronounced nucleation peak. Also, despite using the same deposition current ( $1 \text{ mA cm}^{-2}$ ) in all cells, the nucleation peak ( $\eta_n$ ) varies with  $\sigma$ . Thus, the degree to which the electrode surface is passivated before the start of constant current deposition strongly influence the nucleation peak.

Still, since all samples manage to deposit Li ( $500 \mu\text{Ah cm}^{-2}$  was deposited per sample), they must all have had nucleation of some form. Whether a nucleation peak is visible or not, nucleation must occur as it precedes growth. Because the overpotential affects the rate of nucleation<sup>1</sup>, whether progressive nucleation occurs (where some Li nucleate and start growing while others still nucleate) or instantaneous nucleation occur (where all nuclei nucleate at the same time, and then they all grow) might be the difference seen in Figure 5.1 for different  $\sigma$ . In other words, whether nucleation is more instantaneous or more progressive might depend on whether the deposition curve show a clear nucleation peak or not, respectively. Further support for this idea is given by the nucleation theory, where a larger overpotential for the nucleation,  $|\eta_n|$ , means nucleation of smaller and more nuclei (since  $r \propto \eta^{-1}$  and  $N \propto \eta^3$ ). A larger areal nuclei density after the nucleation means that there are many sites supporting continued growth, lowering the necessity for further nucleation. This is likely as it is more energetically favorable to grow existing nuclei than forming new nuclei. Thus, a sharper dip in cell potential at the nucleation region is indicative of more instantaneous, rather than progressive, nucleation.

---

<sup>1</sup>Since the overpotential affects the nucleation energy barrier, and reaction rates are in general exponentially dependent on the energy barrier.

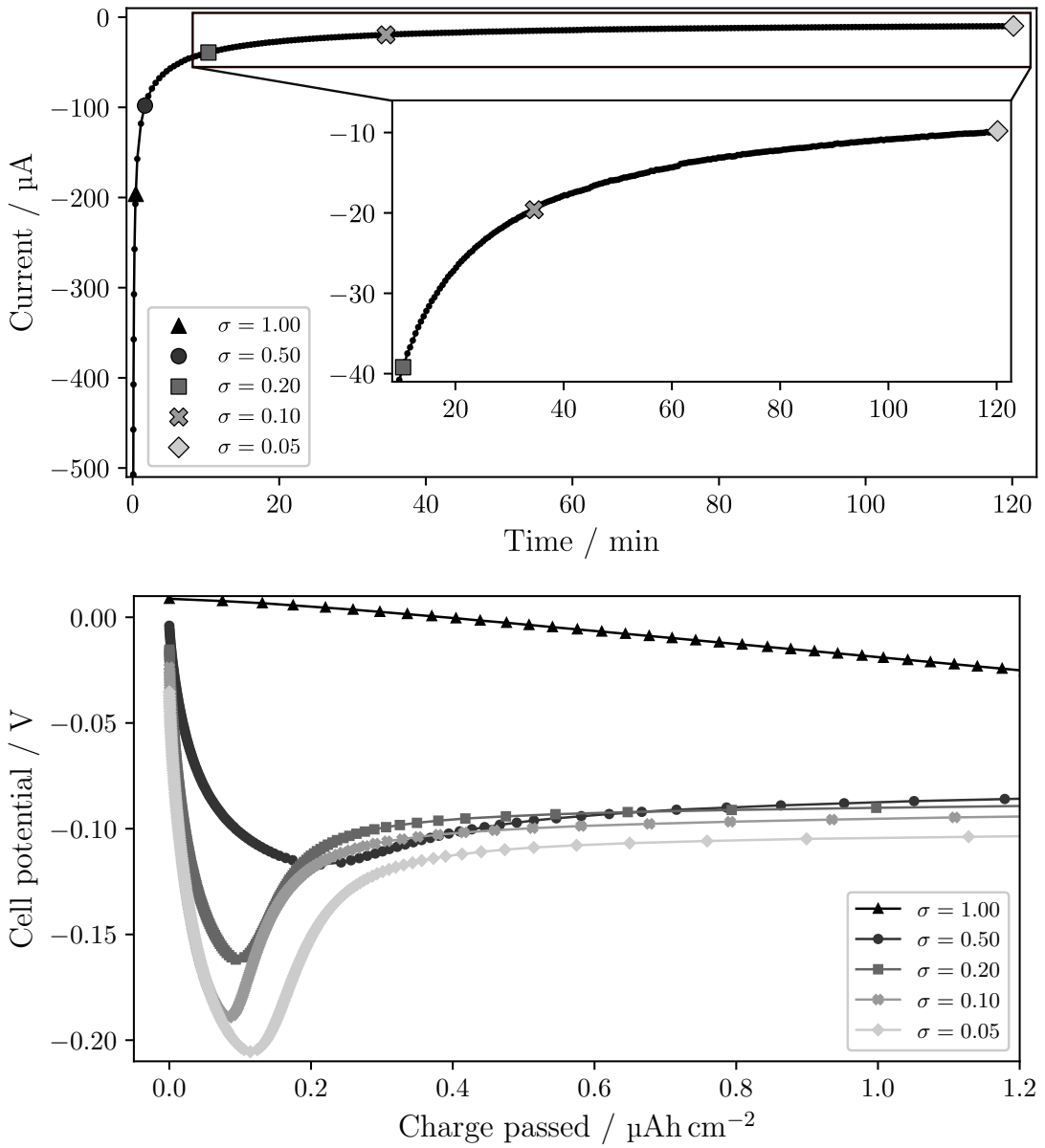


**Figure 5.1.** Top: Current as function of time during the SEI formation by holding 0.010 V in a T-cell. Selected values along this curve are marked, where  $\sigma = I_{\text{SEI-cutoff}}/I_{\text{deposition}}$  (in this case for  $J_{\text{deposition}} = 1 \text{ mA cm}^{-2}$ , or  $I_{\text{deposition}} = 196 \mu\text{A}$ ). Bottom: Cell potential as function of charge passed in said T-cells during the deposition, for different  $\sigma$  and  $J_{\text{deposition}} = 1 \text{ mA cm}^{-2}$ . For large  $\sigma$  (1.00), the applied current drives side reactions to a large proportion, and no nucleation peak is seen. For decreasing  $\sigma$  (0.50, 0.20, 0.10, and 0.05), the nucleation peak becomes more and more pronounced, revealing that weaker side reactions results in nucleation at larger  $|\eta_n|$ .

## 5.2 Deposition current density

The influence of current density was investigated by building and cycling several T-cells, I-cells, and C-cells with different  $J = J_{\text{deposition}}$ . As previously mentioned, in an effort to more accurately compare the deposition curves, the passivation of the Cu surface was performed to  $\sigma = 0.02$  for each respective  $J$  (except for the case  $J = 0.10 \text{ mA cm}^{-2}$  in the T-cell, where  $\sigma = 0.10$  due to  $I_{\text{SEI-cutoff}}$  not reaching  $0.392 \mu\text{A}$  in the T-cell even after several days of passivation). Figure 5.2 compares the deposition curve for different  $J$  for the T-cell, I-cell, and C-cell. Firstly, it is clear that larger  $J$  results in a lower cell potential for both nucleation and growth (larger  $|\eta_n|$  and  $|\eta_p|$ ). Homogenous nucleation theory then implies that the nuclei,  $r \propto \eta^{-1}$ , should be smaller for larger  $J$ , which have been observed in previous experiments [15], [33]. Secondly, the nucleation peak gets less pronounced and disappears for increasing  $J$  in the I-cell and C-cell, but not in the T-cell. For  $J \geq 5 \text{ mA cm}^{-2}$ , the deposition curves for the I-cell and C-cell look more like the deposition curve for  $\sigma = 0.50$  in Figure 5.1. Even though the proportion of deposition current and the current for side reactions were the same ( $\sigma = 0.02$ ) for all  $J$ , the absolute value of  $I_{\text{SEI-cutoff}}$  seems to have been large enough to affect the nucleation for  $J \geq 5 \text{ mA cm}^{-2}$ . To investigate this further, C-cells were cycled with smaller values of  $I_{\text{SEI-cutoff}}$  for different  $J$ , as shown in Figure 5.3. The first case (dashed lines) have  $\sigma = 0.02$ , and the second case (solid lines) have a smaller  $I_{\text{SEI-cutoff}} = 0.392 \mu\text{A}$  for all  $J$ . For each value of  $J$ , the smaller value of  $I_{\text{SEI-cutoff}}$  results in a deposition curve with a clear nucleation peak, indicating that the side reactions did affect the deposition for larger values of  $I_{\text{SEI-cutoff}}$ . This might be due to the fact that a certain time (and charge per electrode area) might be required to form a well passivating SEI layer. When  $\sigma$  is held fixed, an increased deposition current results in less time during formation of the SEI layer. Thus, for  $\sigma = 0.02$  in Figure 5.2, the nucleation becomes more and more progressive (no clear nucleation peak) for increasing deposition current. Also with regard to Figure 5.3, the cell potential in the plateau region is the same for each  $J$  (see Figure B.4 in Appendix B.2). The degree of passivation (choice of  $I_{\text{SEI-cutoff}}$ ) seems therefore to affect the cell potential at nucleation, but not the cell potential during the growth of the Li. This might indicate either that further passivation of the Cu surface occur during the initial deposition, or that the growth of the nuclei is not affected by side reactions in the same way that the initial nucleation is.

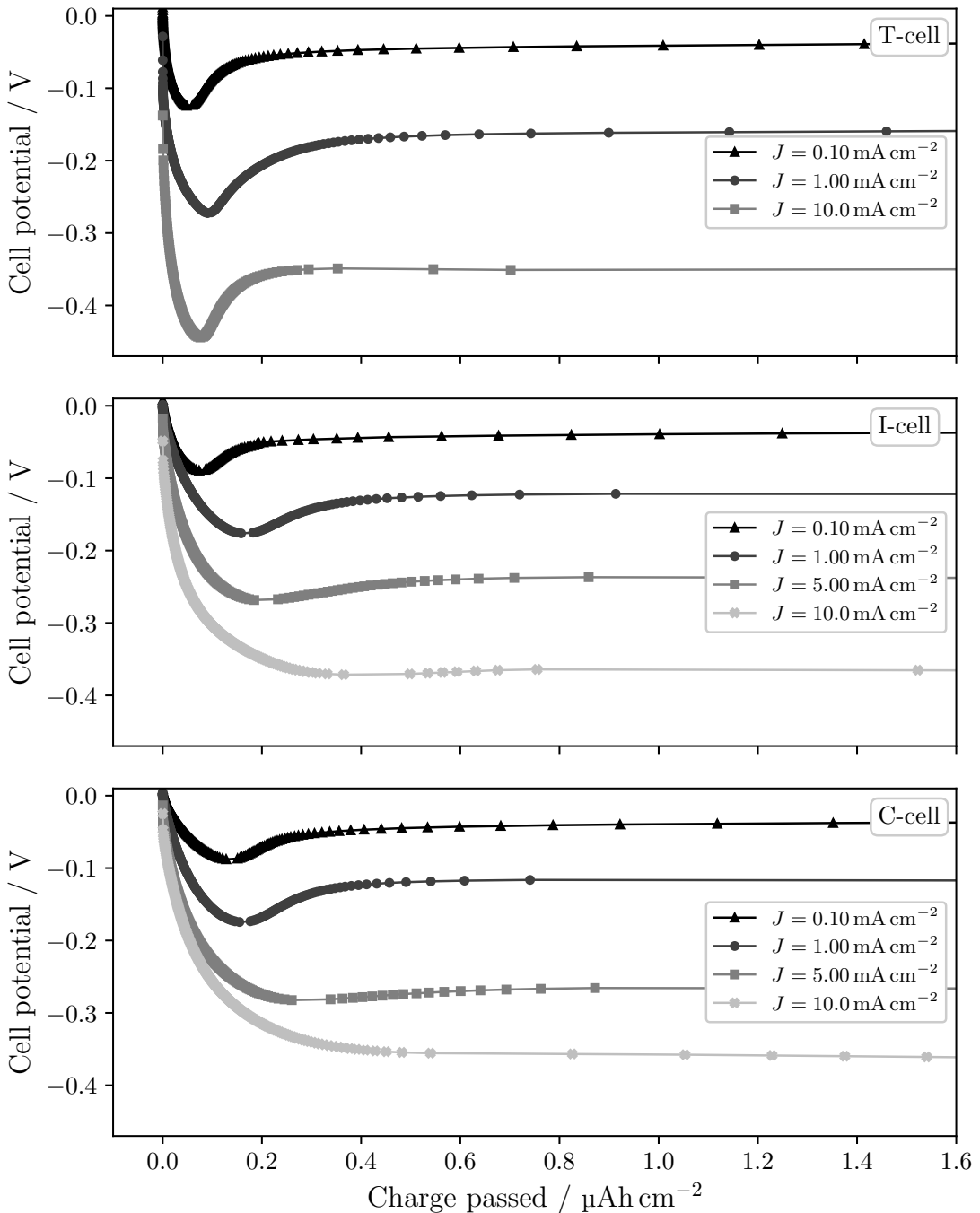


**Figure 5.2.** Comparison of deposition curves for different  $J = J_{\text{deposition}}$  for a given cell configuration. For all measurements,  $\sigma = 0.02$  except  $J = 0.10 \text{ mA cm}^{-2}$  in the T-cell, where  $\sigma = 0.10$ . Larger  $J$  results in larger overpotential in all cell configurations. The nucleation peak disappears for larger  $J$  in the I-cell and C-cell, but not in the T-cell.

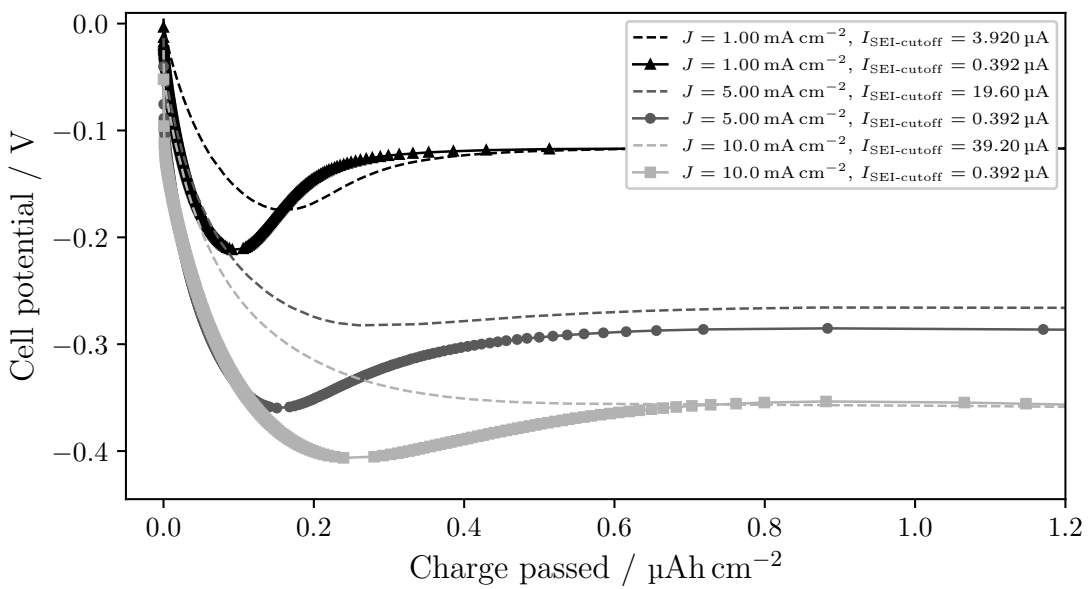


**Figure 5.3.** Comparison of the deposition curves for different  $J = J_{\text{deposition}}$  and  $I_{\text{SEI-cutoff}}$  for the C-cell. Compare the solid curves where  $I_{\text{SEI-cutoff}} = 0.392 \mu\text{A}$ , with the dashed curves where  $\sigma = 0.02$  (different  $I_{\text{SEI-cutoff}}$ ), for each  $J$ . The nucleation peak is more pronounced for smaller  $I_{\text{SEI-cutoff}}$ , while the same cell potential is reached in the growth region (see Figure B.4 for larger values of charge passed).

## 5.3 Comparison of different electrolytes

To see the effect the choice of electrolyte has on nucleation, C-cells were built and cycled with the electrolytes IL, LiPF<sub>6</sub>, and LiFSI. Figure 5.4 shows the current in the C-cells as function of time during the SEI formation by holding a constant cell potential of 0.010 V and the following deposition. Here  $\sigma = 0.02$ , meaning  $I_{\text{SEI-cutoff}} = 3.92 \mu\text{A}$  for  $J_{\text{deposition}} = 1 \text{ mA cm}^{-2}$ . The different electrolytes show the same trend in current versus time, with the IL and LiFSI following each other quite closely. The passivation of the Cu took longer for the LiPF<sub>6</sub> up until a bit before the 10 min mark, where the current decreased faster and reached  $I_{\text{SEI-cutoff}}$  about 5 minute before the two other electrolytes. Moreover, note the difference in timescale for the current in the C-cell compared to the T-cell shown in Figure 5.4. While it took 16 h to reach  $\sigma = 0.02$  in the T-cell, it only took 20 min for the C-cell using the same electrolyte, LiFSI. This is probably mainly due to the difference in electrolyte volume. The larger electrolyte volume in the T-cell means that an increased area is covered where side reactions can occur, resulting in a larger current which takes longer to decrease to  $I_{\text{SEI-cutoff}}$ . Thus, it is reasonable that a larger electrolyte volume results in a longer time to reach a given  $I_{\text{SEI-cutoff}}$  compared to a smaller electrolyte volume. The deposition curves after the SEI formation show similar shape for the IL and LiFSI, while the LiPF<sub>6</sub> went lower in potential but had a less pronounced nucleation peak. Note that the LiPF<sub>6</sub> electrolyte was about six months old (opened 2023-10), and increased impurities due to aging of this electrolyte might be the reason for the difference seen in the deposition curves. There seem to be little difference between the IL and LiFSI electrolyte, and to make a certain claim about the difference seen for the LiPF<sub>6</sub> further measurements are required, preferable with a more fresh electrolyte.

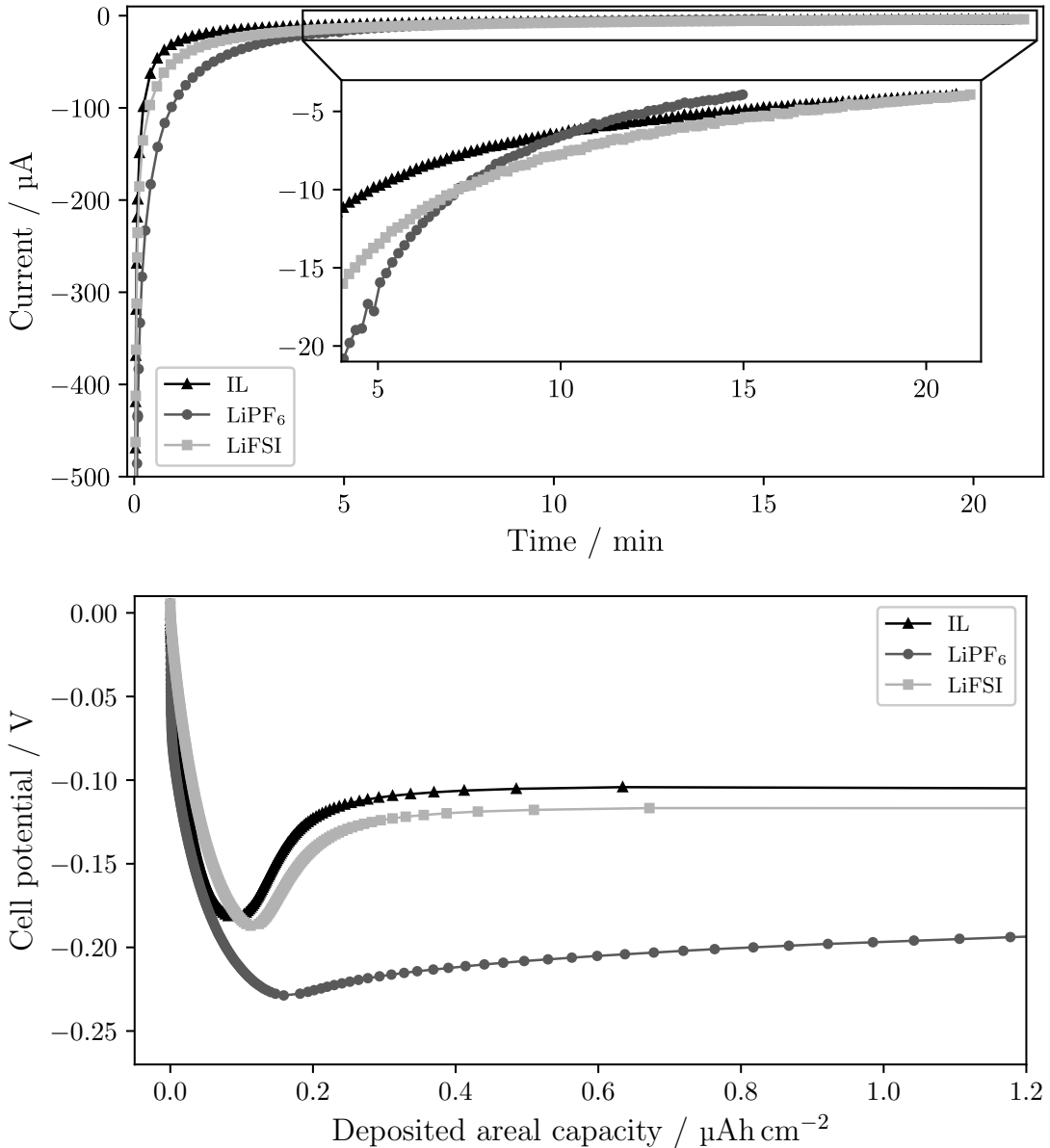


**Figure 5.4.** Top: Current as function of time during the SEI formation by holding 0.010 V in C-cells with different electrolytes. In these cases, about 20 min was necessary to reach  $\sigma = 0.02$  ( $J_{\text{deposition}} = 1 \text{ mA cm}^{-2}$ ), compared to 16 h in the T-cell. Bottom: Comparison of the deposition curve for different electrolytes in the C-cell with  $J_{\text{deposition}} = 1 \text{ mA cm}^{-2}$  and  $\sigma = 0.02$ . The IL and LiFSI are similar, while the difference observed for the LiPF<sub>6</sub> might be due to an aged electrolyte.

## 5.4 Cell configuration and pressure

### 5.4.1 Cell configuration effects on the deposition curve

The influence of cell configuration on the deposition curve was investigated by building and cycling several T-cells, I-cells, and C-cells. Figure 5.5 compares the deposition curve for the different cell configurations for  $J = J_{\text{deposition}}$  equal to  $0.10 \text{ mA cm}^{-2}$ ,  $1.00 \text{ mA cm}^{-2}$ , and  $10.0 \text{ mA cm}^{-2}$ . For these measurements,  $\sigma = 0.02$  (again except for the case  $J = 0.10 \text{ mA cm}^{-2}$  in the T-cell, where  $\sigma = 0.10$ ). The cell voltage is the lowest for the T-cell at the nucleation peak, but similar cell potential is reached at the plateau region. Since the nucleation peak is both more pronounced and reached earlier in the T-cell, this indicates more instantaneous nucleation. Comparing the I-cell to the C-cell, the I-cell reaches the nucleation peak sooner for small  $J$  and with larger overpotential for larger  $J$ . This implies that the difference between even and uneven pressure between the electrodes influences the nucleation behavior. Moreover, compare Figure 5.5 where the nucleation peak is not visible for  $J = 10.0 \text{ mA cm}^{-2}$  with the more pronounced peaks in Figure 5.3 for the same  $J$  but smaller value of  $I_{\text{SEI-cutoff}}$ . Since the T-cell still show a nucleation peak in Figure 5.3 for large  $J$ , the criteria for ending the passivation at  $I_{\text{SEI-cutoff}}$  might have resulted in a better overall passivation in the T-cell compared to the C-cell and I-cell. This could be due to the combined factors of 1) the total current measured during the passivation step is a result from all side reactions, 2) the T-cell have larger volume of electrolyte that covers a larger surface inside the cell, and 3) the thickness of the SEI layer on the Cu surface increases with time. Together, the larger surface area and electrolyte volume in a T-cell results in a larger current from side reactions, making it take a longer time to reach  $I_{\text{SEI-cutoff}}$  in the T-cell. This longer time results in a thicker SEI layer, or more passivation of the Cu surface, in the T-cell compared to the other cell configurations. This might be the explanation behind the visible nucleation peak in the T-cell and not in the C-cell and I-cell for  $J = 10.0 \text{ mA cm}^{-2}$ .

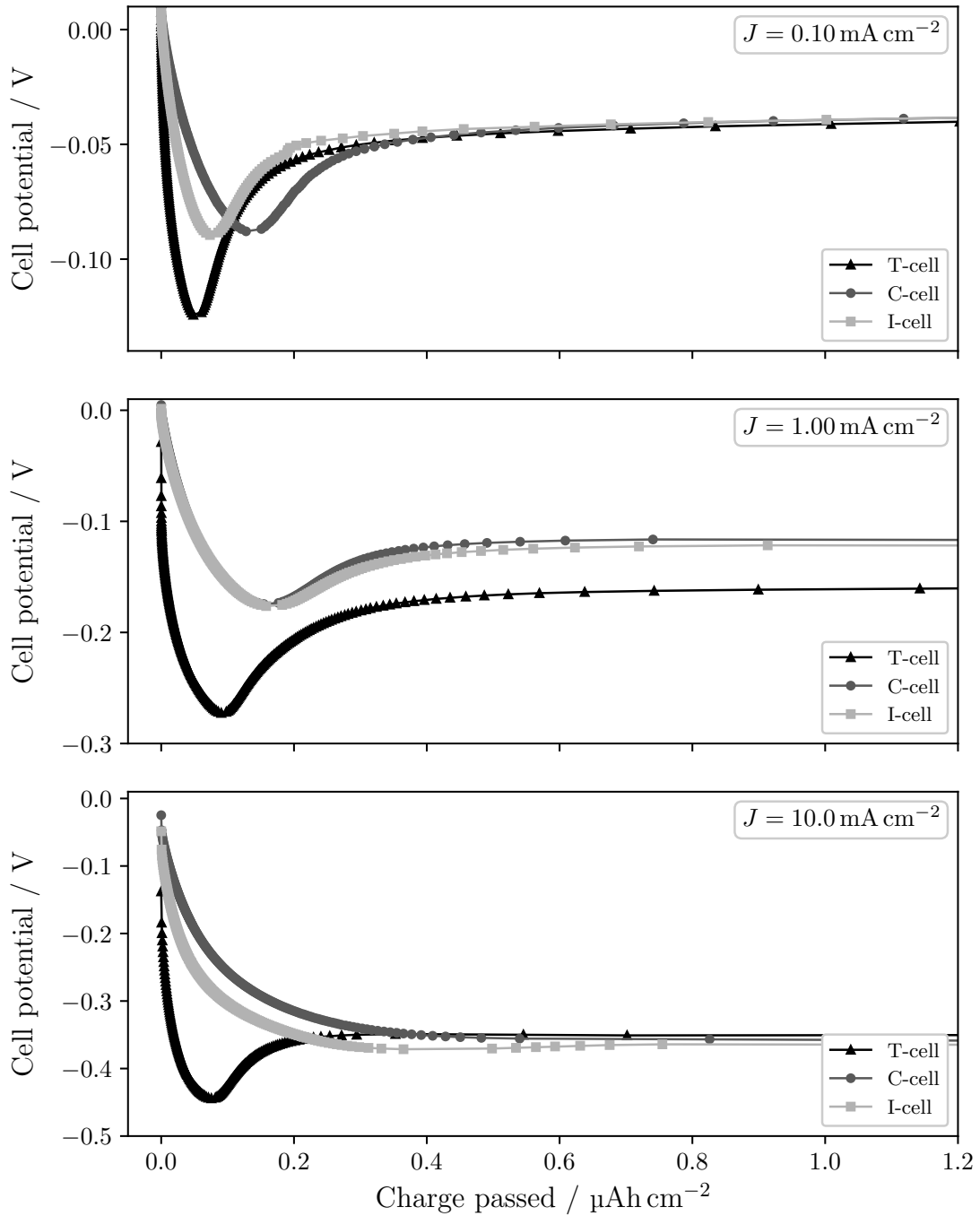


**Figure 5.5.** Comparison of deposition curves for different cell configurations for a given  $J = J_{\text{deposition}}$ . The nucleation peak is most prominent for the T-cell, while the curves look more comparable for the C-cell and I-cell. Despite the T-cell having the largest  $|\eta_n|$ , the  $|\eta_p|$  is more or less the same for all cell configurations for each  $J$ .

### 5.4.2 Pressure effects on the nuclei distribution

To investigate how the pressure between the Li and Cu affects the nucleation, SEM images were captured of the deposited Li in the C-cell and T-cell. The experimental procedures required to obtain clear SEM images of the Li nuclei without remaining electrolyte on the electrode surface are investigated in Appendix B.1. SEM images of deposited Li ( $25 \mu\text{Ah cm}^{-2}$  at  $J_{\text{deposition}} = 1 \text{ mA cm}^{-2}$ ) on Cu in a C-cell at different distances from the center of the deposition are shown in Figure 5.6. The deposition of Li on the Cu can be seen to be non-uniform directly from the photograph as a gray annulus of deposited Li. The annulus shape means there is little to no Li at its center and significantly more along the outer edge of the annulus. Looking at the SEM images, it is clear that the morphology of the Li varies, from (a) crystalline nuclei closer to the center and becoming (c) larger, flatter "islands" further away. Thus, the deposition of Li in a C-cell is uneven and the morphology depends on the radial position. The nuclei areal density  $N$  decreases as the typical size  $r$  of the nuclei increases moving from (a) to (c). More specifically,  $N_{(a)} = 0.024 \text{ nuclei } \mu\text{m}^{-2}$  with a characteristic size (diameter)  $2r_{(a)} = 1 \mu\text{m}$  to  $1.5 \mu\text{m}$  of the crystalline nuclei. The nuclei are visibly larger in (b) and (c), with  $N_{(b)} = 0.022 \text{ nuclei } \mu\text{m}^{-2}$  and  $2r_{(b)} = 2 \mu\text{m}$  to  $3 \mu\text{m}$ , while  $N_{(c)} = 0.016 \text{ nuclei } \mu\text{m}^{-2}$  with  $2r_{(c)} \geq 4 \mu\text{m}$ , with large variation in the upper limit in  $2r_{(c)}$  since that depends on the number of nuclei which seem to have joined together. This behavior qualitatively follows the theoretical relations derived using homogenous nucleation theory. Since  $r_{\text{critical}} \propto \eta^{-1}$ , the smaller crystalline nuclei would have formed at a larger  $|\eta|$  while the larger "islands" could have nucleated at smaller  $|\eta|$ . In other words, the crystalline nuclei probably nucleated at the nucleation peak, while the "islands" nucleated after that. Another set of SEM images were obtained in the C-cell to explore if the angular position also matters. Figure 5.7 compares SEM images of deposited Li ( $50 \mu\text{Ah cm}^{-2}$  at  $J_{\text{deposition}} = 1 \text{ mA cm}^{-2}$ ) on Cu in a C-cell at different angular positions along the edge of the deposition. The morphology ranges from mostly bush-like growth to mostly round nuclei. Thus, the morphology of deposited Li depends not only on the radial position, but also on the angular position along the edge of the deposition. This can be explained by a finding by [30], which showed that the pressure inside a C-cell is uneven due to the wave spring, resulting in low pressure in the center and high pressure at larger radii. This supports both the radial variation in Li morphology seen in Figure 5.6 with less deposition at the center and more at larger radii, and the angular variation seen in Figure 5.7 due to the wave spring applying more pressure at certain points. In summary, the radial and angular variations are likely due to uneven pressure from the wave spring in the C-cell, where areas of low pressure result in less deposition and areas of higher pressure results in more deposition.

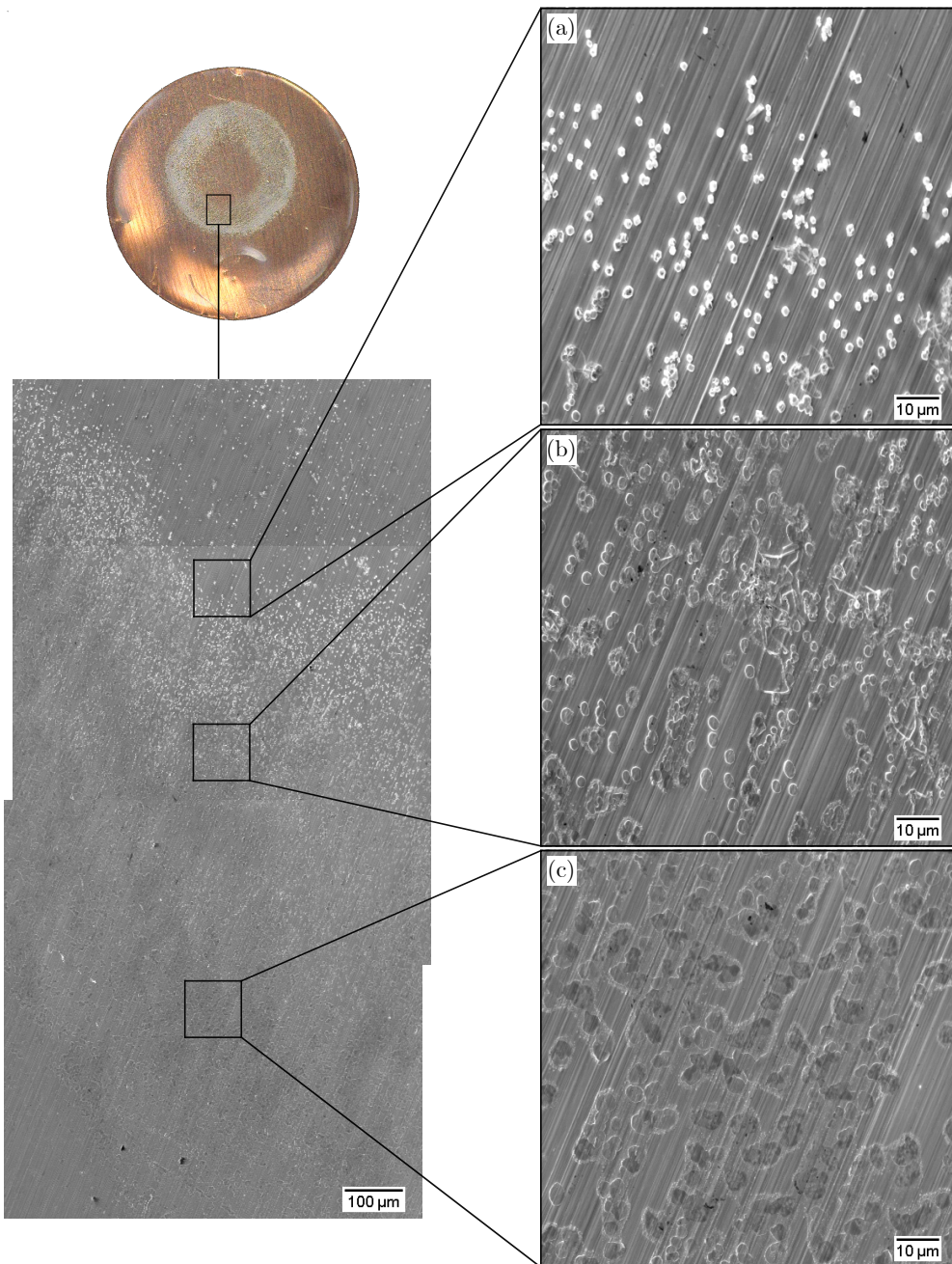


**Figure 5.6.** Different Li morphologies along the radius for the C-cell. The upper left photograph shows deposited Li (gray annulus) on Cu. The black rectangle on the Cu illustrates the position of the SEM images, which on the left-hand side have been overlaid (matching the features on one image with the features on the others). The SEM images on the right-hand side are magnifications of the ones on the left-hand side, showing different Li morphologies, from (a) small crystalline nuclei to (c) larger and flatter "islands", at different positions along the radius of the deposition.

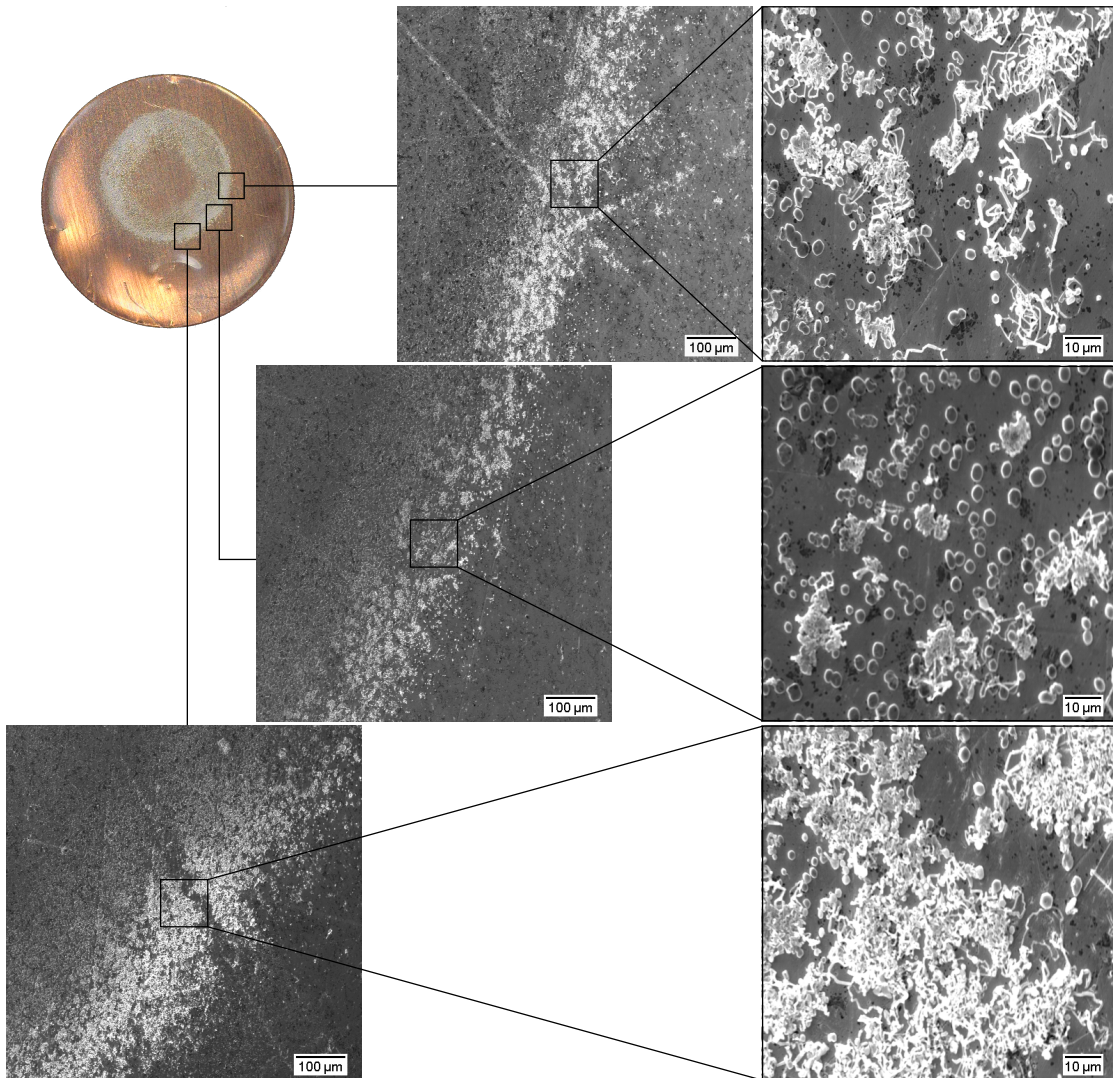


**Figure 5.7.** Different morphologies at the edge of the Li deposition for the C-cell. The upper left photograph shows deposited Li (gray annulus) on Cu. The black squares on the Cu illustrate the positions of the SEM images. The SEM images on the right-hand side are magnifications of the ones to the left. Different Li morphologies, round nuclei or bush-like growth, are observed at different angular positions along the edge of the deposition.

Having seen the effect of pressure in the C-cell, the absence of pressure between the electrode materials was investigated using the T-cell. Figure 5.8 shows SEM images of deposited Li ( $30 \mu\text{Ah cm}^{-2}$  at  $J_{\text{deposition}} = 1 \text{ mA cm}^{-2}$ ) on Cu in a T-cell at different positions. The Li is more evenly distributed compared to in a C-cell, with a more similar morphology observed throughout the deposited area. This further corroborates that pressure influences the deposition. Moreover, the morphology is in this case mainly a mixture of crystalline nuclei and needle-like growth, compared to the flatter "islands" and bush-like growth in the C-cell. This finding is supported by simulations made by [34], which showed that the absence of applied pressure results in more thin growth upwards from the substrate compared to with added pressure. While the "islands" are not observed in the T-cell, the needle-like growth could be conceived as a precursor to the bush-like growth. The needle-like growth seen in Figure 5.8 might thus evolve into the bush-like growth seen in Figure 5.7 as the amount of deposited Li increases. This idea is supported by earlier experiments [35].

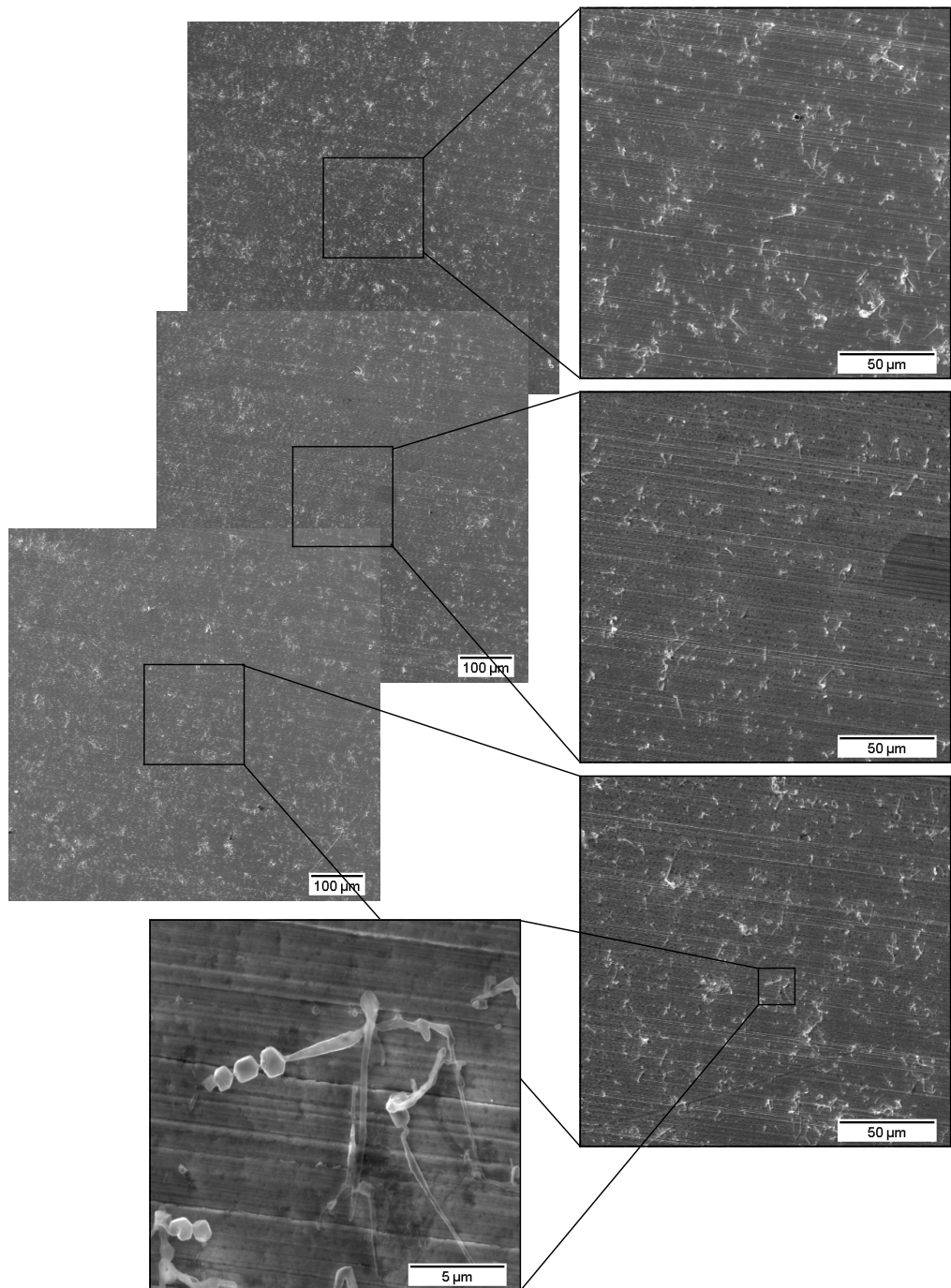


**Figure 5.8.** The deposition of Li in a T-cell is much more evenly distributed and with similar morphology over a larger distance compared to the C-cell (Figure 5.6 and Figure 5.7). The left-hand side shows overlaid SEM images, and the magnified images to the right are representative over the entire area of the deposition. The highest magnification image shows that the Li morphology is a combination of smaller crystalline nuclei about 1  $\mu\text{m}$  in diameter, together with long and thin needle-like structures.



# 6

## Conclusions

The electrochemical nucleation of Li on Cu have been investigated using electrochemical cycling and SEM imaging. Firstly, the deposition curve depends strongly on the ratio  $\sigma = I_{\text{SEI-cutoff}}/I_{\text{deposition}}$  of the current at the end of the SEI formation,  $I_{\text{SEI-cutoff}}$ , and the current used during deposition,  $I_{\text{deposition}}$ . The nucleation peak becomes more pronounced with larger overpotential for decreasing  $\sigma$ . Conversely, no nucleation peak was observed for sufficiently large  $\sigma$ . Thus, the balance between the current driving side reactions and the current driving is essential for influencing whether the nucleation is more instantaneous or progressive. Secondly, for high deposition currents,  $\sigma = 0.02$  was found to result in a too high  $I_{\text{SEI-cutoff}}$ , where the nucleation peak did not appear. However, for lower  $I_{\text{SEI-cutoff}}$  at the same  $J$ , the nucleation peak was observed. Thus, the choice of  $I_{\text{SEI-cutoff}}$  is highly influential on the shape of the nucleation peak, and having a constant  $\sigma$  for a large range of different deposition current densities seems to be a suboptimal method for comparing the nucleation behavior. Thirdly, the uneven pressure distribution in the C-cell caused by the wave spring resulted in deposition of Li in the shape of an annulus, with less deposition in areas of low pressure and more deposition in areas of high pressure. Moreover, the morphology of the Li changed with both the radial and angular position in the deposition. The observed morphology ranged from small crystalline nuclei, to larger and flatter "islands", and bush-like growth. Therefore, a uniform pressure distribution between the electrode materials is essential to achieve uniform deposition in LMBs.



## References

- [1] B. Scrosati, K. M. Abraham, and W. van Schalkwijk, *Lithium Batteries: Advanced Technologies and Applications*. Wiley, 2013, ISBN: 9781118183656.
- [2] K. W. Beard, *Linden's Handbook of Batteries*, 5th ed. Mc Graw Hill, 2019, ISBN: 978-1-260-11592-5.
- [3] C. Xu, Q. Dai, L. Gaines, M. Hu, A. Tukker, and B. Steubing, “Future material demand for automotive lithium-based batteries,” *Communications Materials*, vol. 1, no. 99, 2020-10. DOI: <https://doi.org/10.1038/s43246-020-00095-x>.
- [4] B. V. Ratnakumar, M. C. Smart, R. C. Ewell, L. D. Whitcanack, K. B. Chin, and S. Surampudi, *Lithium-ion rechargeable batteries on mars rover*, version V1, 2004. DOI: 2014 / 38818. [Online]. Available: <https://hdl.handle.net/2014/38818>.
- [5] *Batteries for space power systems*, <https://ntrs.nasa.gov/citations/19690008710>, Report number: NASA-SP-172, Available online: <https://ntrs.nasa.gov/api/citations/19690008710/downloads/19690008710.pdf> (accessed: 2024-01-17), NASA, 1968-01.
- [6] B. Scrosati and J. Garche, “Lithium batteries: Status, prospects and future,” *Journal of Power Sources*, vol. 195, no. 9, pp. 2419–2430, 2010, ISSN: 0378-7753. DOI: <https://doi.org/10.1016/j.jpowsour.2009.11.048>.
- [7] J. Deng, C. Bae, A. Denlinger, and T. Miller, “Electric vehicles batteries: Requirements and challenges,” *Joule*, vol. 4, no. 3, pp. 511–515, 2020, ISSN: 2542-4351. DOI: <https://doi.org/10.1016/j.joule.2020.01.013>.
- [8] D. Lin, Y. Liu, and Y. Cui, “Reviving the lithium metal anode for high-energy batteries,” *Nature Nanotechnology*, vol. 12, pp. 194–206, 2017-03. DOI: <https://doi.org/10.1038/nnano.2017.16>.

## References

---

- [9] C. Fang, B. Lu, G. Pawar, M. Zhang, D. Cheng, and S. Chen, “Pressure-tailored lithium deposition and dissolution in lithium metal batteries,” *Nature Energy*, vol. 6, pp. 987–994, 2021-10. DOI: 10.1038/s41560-021-00917-3.
- [10] X. Shen, R. Zhang, P. Shi, X. Chen, and Q. Zhang, “How does external pressure shape li dendrites in li metal batteries?” *Advanced Energy Materials*, vol. 11, no. 10, 2021-01. DOI: 10.1002/aenm.202003416.
- [11] M. Sadd, S. Xiong, J. Bowen, F. Marone, and A. Matic, “Investigating microstructure evolution of lithium metal during plating and stripping via operando x-ray tomographic microscopy,” *Nature Communications*, vol. 14, no. 854, 2023-02. DOI: 10.1038/s41467-023-36568-z.
- [12] J. Qian, W. A. Henderson, W. Xu, *et al.*, “High rate and stable cycling of lithium metal anode,” *Nature Communications*, vol. 6, no. 6362, 2015-02. DOI: <https://doi.org/10.1038/ncomms7362>.
- [13] Z. Huang, G. Zhou, W. Lv, *et al.*, “Seeding lithium seeds towards uniform lithium deposition for stable lithium metal anodes,” *Nano Energy*, vol. 61, pp. 47–53, 2019-06. DOI: <https://doi.org/10.1016/j.nanoen.2019.04.036>.
- [14] X. Xieyu, J. Xingxing, K. O. O, *et al.*, “Diffusion limited current density: A watershed in electrodeposition of lithium metal anode,” *Advanced Energy Materials*, vol. 12, no. 19, p. 2200244, 2022-05. DOI: <https://doi.org/10.1002/aenm.202200244>.
- [15] A. Pei, G. Zheng, F. Shi, Y. Li, and Y. Cui, “Nanoscale nucleation and growth of electrodeposited lithium metal,” *Nano Letters*, vol. 17, no. 2, pp. 1132–1139, 2017-01. DOI: 10.1021/acs.nanolett.6b04755.
- [16] L. Qin, Y. Wu, M. Shen, *et al.*, “Straining copper foils to regulate the nucleation of lithium for stable lithium metal anode,” *Energy Storage Materials*, vol. 44, pp. 278–284, 2022, ISSN: 2405-8297. DOI: <https://doi.org/10.1016/j.ensm.2021.10.028>.
- [17] T. Balamurugan, H. T. Teka, H. Chen-Jui, *et al.*, “Nucleation and growth mechanism of lithium metal electroplating,” *Journal of the American Chemical Society*, vol. 141, no. 46, pp. 18 612–18 623, 2019. DOI: 10.1021/jacs.9b10195.
- [18] O. Crowther and A. C. West, “Effect of electrolyte composition on lithium dendrite growth,” *Journal of The Electrochemical Society*, vol. 155, no. A806, 2008. DOI: 10.1149/1.2969424.

- [19] A. Allerhand, “Who invented the earliest capacitor bank (“battery” of leyden jars)? it’s complicated,” *Proceedings of the IEEE*, vol. 106, no. 3, pp. 496–503, 2018. DOI: 10.1109/JPROC.2018.2795846.
- [20] M. V. Reddy, A. Mauger, C. M. Julien, A. Paolella, and K. Zaghib, “Brief history of early lithium-battery development,” *Materials*, vol. 13, no. 8, p. 1884, 2020-04. DOI: 10.3390/ma13081884.
- [21] *Cell*, Merriam-Webster.com Dictionary, (accessed: 2024-02-13). [Online]. Available: <https://www.merriam-webster.com/dictionary/cell>.
- [22] E. Andersson. “Spectroelectrochemical analysis of the li-ion battery solid electrolyte interphase using simulated raman spectra.” Uppsala Universitet, ISSN: 1401-5773. (2020-06), [Online]. Available: <https://www.diva-portal.org/smash/get/diva2:1442076/FULLTEXT01.pdf> (visited on 2024-03-25).
- [23] W. Zhang, E. Hosono, D. Asakura, *et al.*, “Chemical-state distributions in charged licoo<sub>2</sub> cathode particles visualized by soft x-ray spectromicroscopy,” *Scientific Reports*, vol. 13, no. 4639, 2023-03. DOI: 10.1038/s41598-023-30673-1.
- [24] “Characteristics of lithium-ion batteries.” (2024), [Online]. Available: <http://www.electricity-magnetism.org/electric-battery/characteristics-of-lithium-ion-batteries/> (visited on 2024-03-25).
- [25] A. J. Bard, L. R. Faulkner, and H. S. White, *Electrochemical Methods: Fundamentals and Applications*, 3rd ed. Wiley, 2022-05, ISBN: 978 111 933 4064.
- [26] M. Winter, B. Barnett, and K. Xu, “Before li ion batteries,” *Chemical reviews*, vol. 118, no. 23, pp. 11 433–11 456, 2018-11. DOI: 10.1021/acs.chemrev.8b00422.
- [27] X.-B. Cheng, R. Zhang, C.-Z. Zhao, and Q. Zhang, “Toward safe lithium metal anode in rechargeable batteries: A review,” *Chemical Reviews*, vol. 117, no. 15, pp. 10 403–10 473, 2017-07. DOI: <https://doi.org/10.1021/acs.chemrev.7b00115>.
- [28] Y. Xu, K. Dong, Y. Jie, *et al.*, “Promoting mechanistic understanding of lithium deposition and solid-electrolyte interphase (sei) formation using advanced characterization and simulation methods: Recent progress, limitations, and future perspectives,” *Advanced Energy Materials*, vol. 12, no. 19, p. 2200398, 2022. DOI: <https://doi.org/10.1002/aenm.202200398>.
- [29] G. Feng, Y. Shi, H. Jia, *et al.*, “Progressive and instantaneous nature of lithium nucleation discovered by dynamic and operando imaging,” *Science Advances*, vol. 9, no. 21, eadg6813, 2023. DOI: 10.1126/sciadv.adg6813.

## References

---

- [30] C. Soulen, N. Lam, J. Holoubek, and P. Liu, “Bridging the gap between pouch and coin cell electrochemical performance in lithium metal batteries,” *Journal of The Electrochemical Society*, vol. 171, no. 2, p. 020535, 2024-02. DOI: [10.1149/1945-7111/ad2731](https://doi.org/10.1149/1945-7111/ad2731).
- [31] V. Borovytsky, “Huygens–fresnel principle and abbe formula,” *Optical Engineering*, vol. 57, no. 9, 2019-09. DOI: <https://doi.org/10.1117/1.OE.57.9.095104>.
- [32] K. Vernon-Parry, “Scanning electron microscopy: An introduction,” *III-Vs Review*, vol. 13, no. 4, pp. 40–44, 2000, ISSN: 0961-1290. DOI: [https://doi.org/10.1016/S0961-1290\(00\)80006-X](https://doi.org/10.1016/S0961-1290(00)80006-X).
- [33] L. Que and W. Chen, “Analysis of the lithium electrodeposition behavior in the charge process of lithium metal battery associated with overpotential,” *Journal of Power Sources*, vol. 557, p. 232536, 2023, ISSN: 0378-7753. DOI: <https://doi.org/10.1016/j.jpowsour.2022.232536>. [Online]. Available: <https://www.sciencedirect.com/science/article/pii/S0378775322015130>.
- [34] X. Shen, R. Zhang, P. Shi, X. Chen, and Q. Zhang, “How does external pressure shape li dendrites in li metal batteries?” *Advanced Energy Materials*, vol. 11, no. 10, 2021-01, ISSN: 1614-6840. DOI: [10.1002/aenm.202003416](https://doi.org/10.1002/aenm.202003416).
- [35] J. Steiger, D. Kramer, and R. Mönig, “Microscopic observations of the formation, growth and shrinkage of lithium moss during electrodeposition and dissolution,” *Electrochimica Acta*, vol. 136, pp. 529–536, 2014, ISSN: 0013-4686. DOI: <https://doi.org/10.1016/j.electacta.2014.05.120>.
- [36] L. Gehrlein, “Enhancing the performance of si/gr anodes by evaluating the impact of electrolyte formulations on the solid electrolyte interphase,” 38.02.01; LK 01, Ph.D. dissertation, Karlsruher Institut für Technologie (KIT), 2022, 170 pp. DOI: [10.5445/IR/1000151010](https://doi.org/10.5445/IR/1000151010).

# A |

## **Supplementary information: methods**

### **A.1 Polishing of Cu**

Figure A.1 shows the polishing of the 70 mm × 70 mm Cu sheet on the turntable. First, two edges of the Cu sheet were bent around the edges of a flat piece of square glass. A grinding paper was then placed center on the turntable (Buehler Beta grinder-polisher) and the water was turned on. During polishing, the grinding paper rotated while the Cu sheet was held in place by applying pressure on the edges of the glass using the fingers. An even surface polish was achieved by using the fingers to apply pressure on top of the glass in spots that at first received less grinding. Once an even surface polish was achieved for a given grinding paper, the next grinding paper was used. The following silicon carbide grinding papers from Beuhler were used: P1200, P2500, and P4000, in order of polishing from coarser to finer. After the finest grinding paper, the Cu was blown dry using N<sub>2</sub> gas, put in a new plastic bag and sealed. Then followed the punching and cleaning as described in subsection 4.1.1.

Appendix A. Supplementary information: methods

---

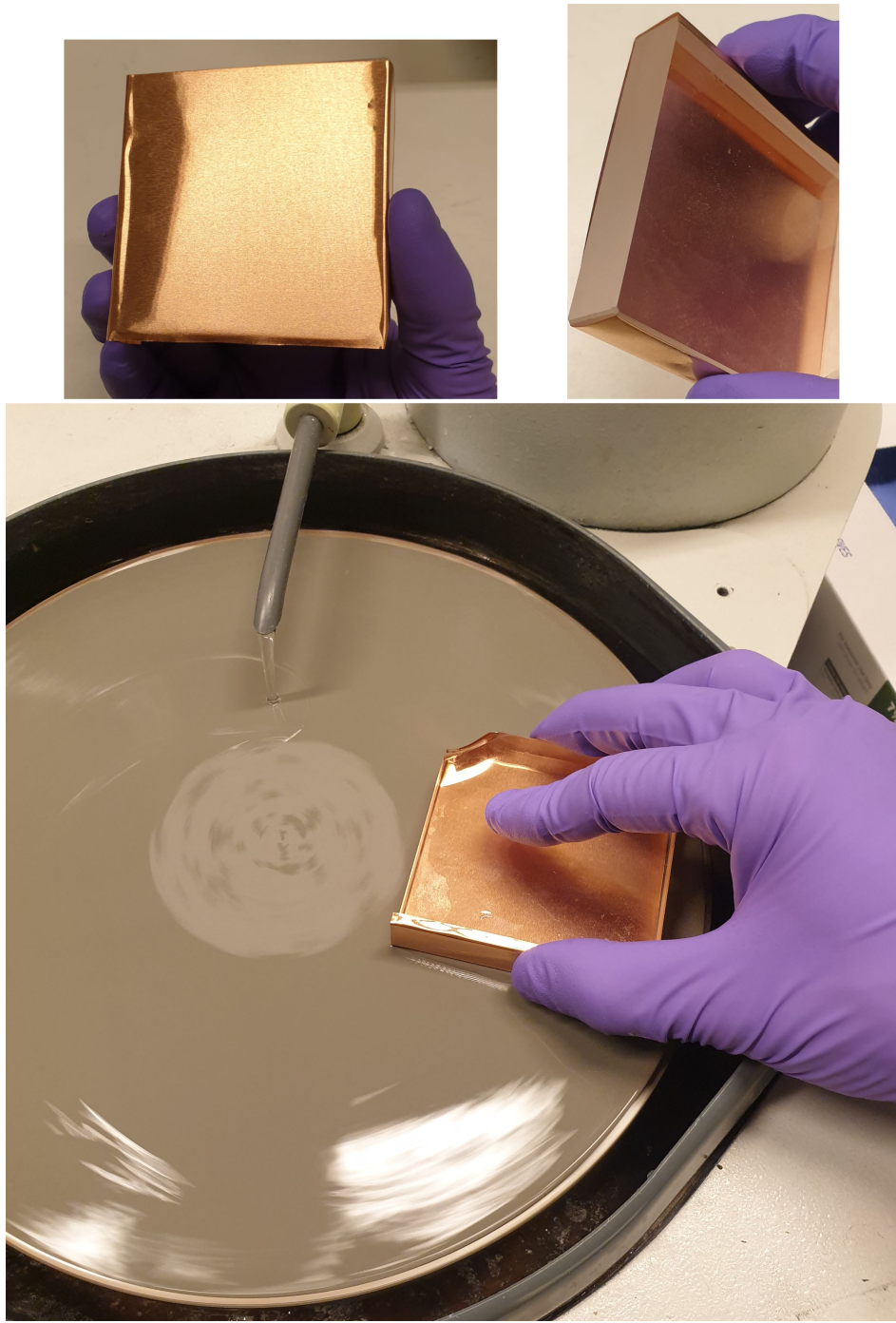


**Figure A.1.** Polishing of a Cu sheet using a turntable. See text for details.

## A.2 Polypropylene spacer for T-cell

Figure A.2 shows the process of creating the 1 mm thick horseshoe-shaped spacers of PP. A cut was made with a scalpel from the edge of a 1 mm thick sheet of PP. A puncher 10 mm in diameter were used (along with a persuasive hammer) to punch out a circular piece where the cut was made. The piece was laid on the wooden board and another puncher, this time 7 mm in diameter, was centered and used to punch out the middle part. Due to the puncher being cone-shaped, the circular piece of PP expanded along the perimeter when the inner part was punched. Therefore, the cut done in the first step allows the PP piece to expand without becoming damaged during the last punching step. This worked significantly better than punching without a cut. Moving on, a few millimeters of the ring was cut away using a scalpel, creating an opening to inject the electrolyte when assembling the T-cell. Finally, a scalpel was used to clean up the edges.



**Figure A.2.** The process of punching the PP spacers. See text for explanation.

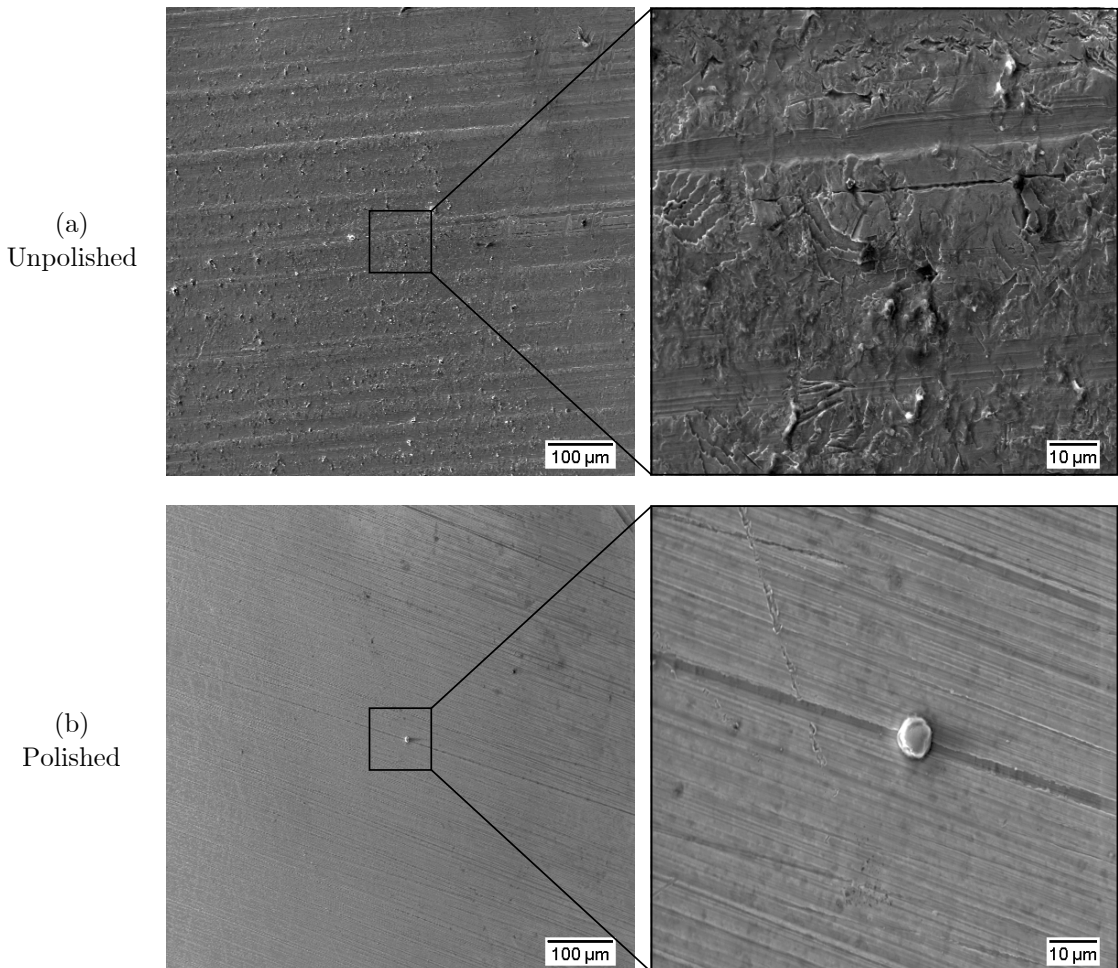


# B

## Supplementary information: results

### B.1 Experimental procedures to obtain clean SEM images of Li nuclei

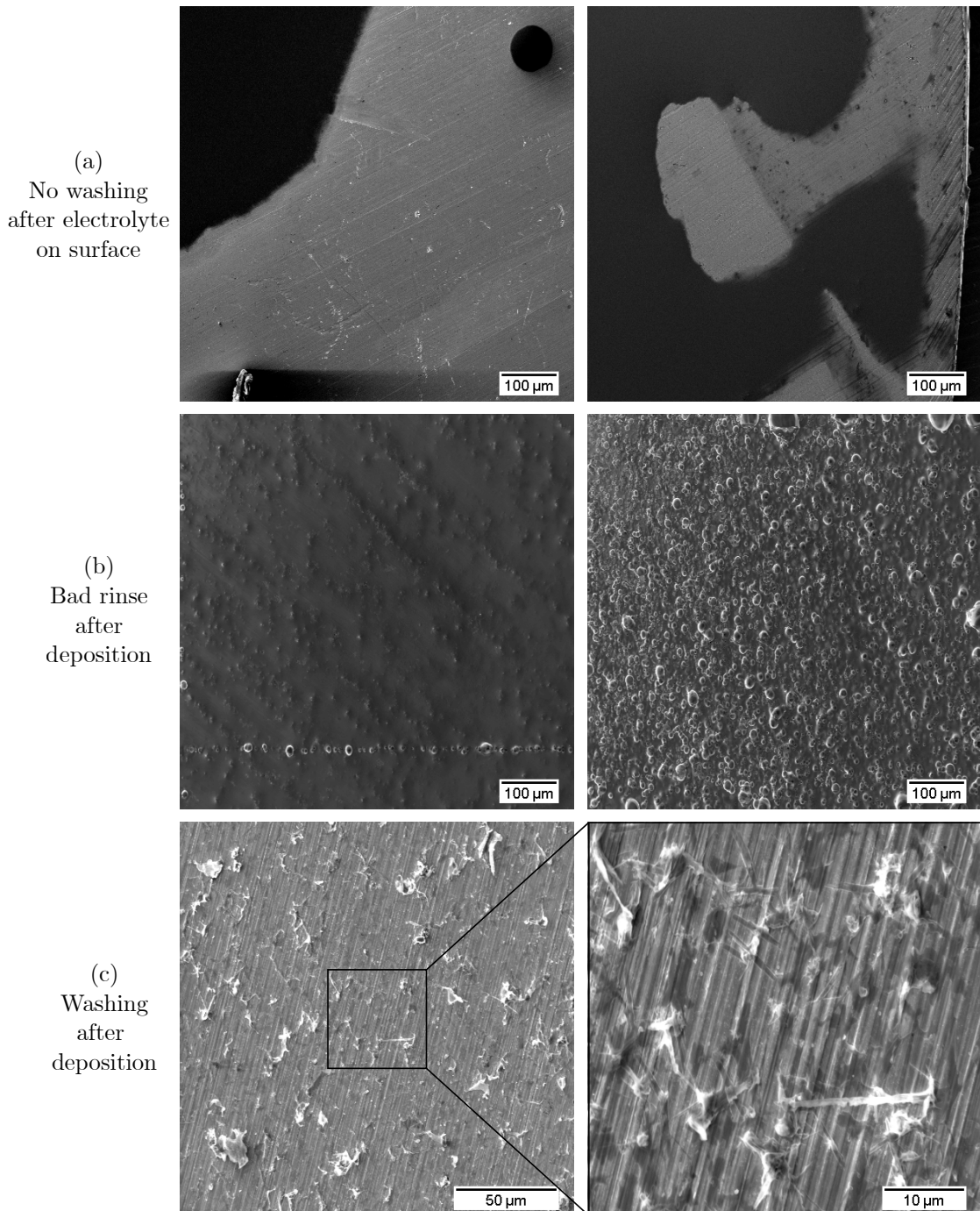
To clearly image the Li nuclei distribution, it was necessary to investigate sample preparation before measurement in the SEM. SEM images were obtained of an unpolished and a polished Cu surface, and also of the Cu surface for various treatments after deposition. Figure B.1 shows SEM images of an unpolished and a polished piece of Cu with some deposited Li. The unpolished surface looks rough, while the polished is significantly smoother. To minimize the influence of a rough surface during the nucleation and making it easier to separate the deposited Li from the surface features, the Cu surface should be polished. After deposition of Li, the Cu electrode was treated in various ways before being measured in the SEM. Figure B.2 compares SEM images of Cu surfaces with no washing, rinsing, and washing by immersion. First, no washing after having put only LiFSI electrolyte on the Cu surface leaves large dark areas of electrolyte that obstruct the view. Secondly, a bad rinse with DME after deposition of Li can leave behind large dark areas on the surface that seem to cover the deposited Li underneath. The dark areas reacted with the electron beam and started to bubble when imaged. Thirdly, deposited Li ( $50 \mu\text{Ah cm}^{-2}$  at  $J_{\text{deposition}} = 1 \text{ mA cm}^{-2}$ ) was clearly observed in the SEM after immersing and letting the Cu rest for 1 min in DME. However, some of the deposited Li might have had time to react in the DME bath, seemingly leaving behind smaller localized dark spots. Other washing times were tested, 10 s and 5 min. The shortest duration of 10 s failed to remove all large dark areas, while the longer 5 min immersion showed little improvement over the 1 min immersion.



**Figure B.1.** SEM images of (a) an unpolished and (b) a polished Cu surface with some deposited Li. The polished Cu have substantially smaller surface roughness compared to the unpolished surface, resulting in easier identification of deposited Li and a clearer image.

Thus, washing of the surface was necessary and the immersion in DME for 1 min was deemed the best, showing sufficient removal of electrolyte while minimizing the potential reaction of deposited Li with the washing solvent. This finding is in agreement with [36] which found that a 1 min wash resulted in less variation in removed species compared to rinsing the substrate. In short, for clear and clean SEM images, the Cu surface should be polished to minimize surface roughness and washed by a 1 min immersion in DME after deposition of Li.

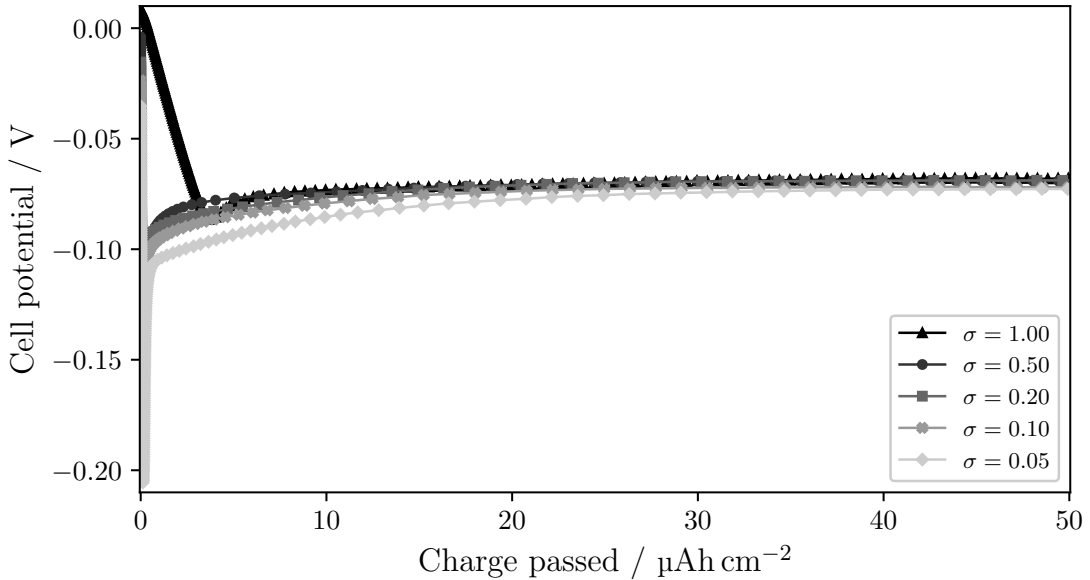
### B.1. Experimental procedures to obtain clean SEM images of Li nuclei



**Figure B.2.** SEM images of Cu surfaces after various treatments. (a) No washing leaves large dark parts of electrolyte that covers and obscure the surface beneath it. (b) A bad rinse of DME can leave enough electrolyte on the surface such that it bubbles when exposed to the electron beam (images taken at the same place at different times). (c) Washing by immersion for 1 min in DME results in no large dark parts, however smaller dark spots can be seen, which could be deposited Li that have reacted.

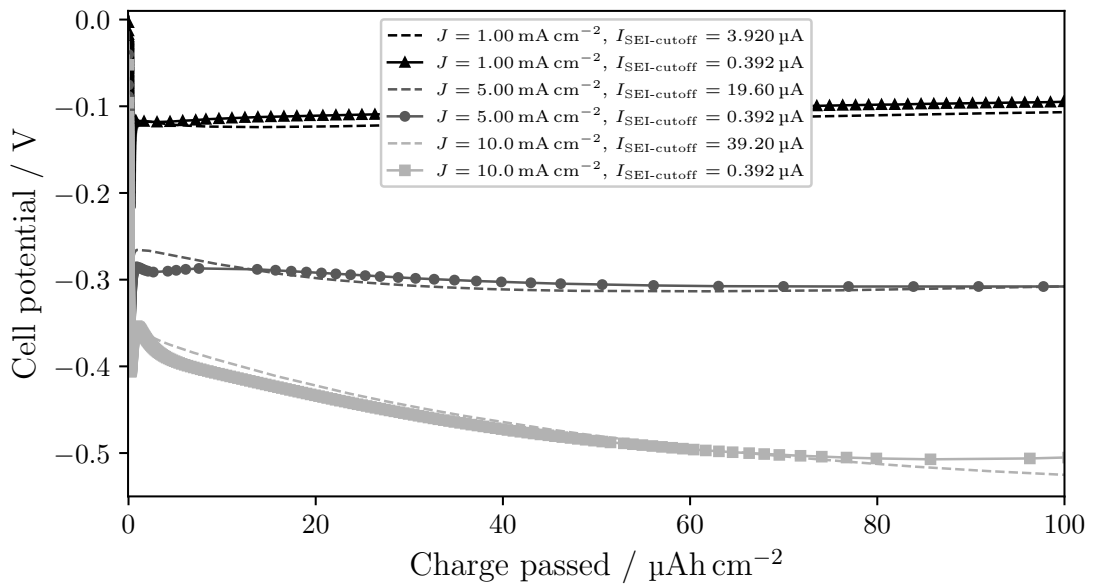
## B.2 Influence of passivation of the Cu surface before deposition

Figure B.3 shows the same data as in the bottom part of Figure 5.1 but for larger values of charge passed. More or less the same cell potential is reached in the plateau region, regardless of the value of  $\sigma$ .



**Figure B.3.** Cell potential as function of charge passed in T-cells during deposition, for different  $\sigma$  at  $J_{\text{deposition}} = 1 \text{ mAh cm}^{-2}$ .

Figure B.4 shows the same data as in Figure 5.3 but for larger values of charge passed. Despite the deposition curves (for a given  $J = J_{\text{deposition}}$ ) having different shapes at the nucleation region (see Figure 5.3), they reach more or less the same cell potential in the plateau region. This supports the idea that the different  $I_{\text{SEI-cutoff}}$  primarily affects the nucleation behavior rather than the growth.



**Figure B.4.** Comparison of the deposition curves for different  $J = J_{\text{deposition}}$  and  $I_{\text{SEI-cutoff}}$  for the C-cell. Note that despite having different  $I_{\text{SEI-cutoff}}$ , the curve pair for each  $J$  reach more or less the same cell potential in the plateau region.



**DEPARTMENT OF PHYSICS**  
**CHALMERS UNIVERSITY OF TECHNOLOGY**  
Gothenburg, Sweden  
[www.chalmers.se](http://www.chalmers.se)



**CHALMERS**  
UNIVERSITY OF TECHNOLOGY